

# Quality-controlled meteorological datasets from SIGMA automatic weather stations in northwest Greenland, 2012–2020

Motoshi Nishimura<sup>1\*</sup>, Teruo Aoki<sup>1</sup>, Masashi Niwano<sup>2</sup>, Sumito Matoba<sup>3</sup>, Tomonori Tanikawa<sup>2</sup>, Tetsuhide Yamasaki<sup>4</sup>, Satoru Yamaguchi<sup>5</sup>, Koji Fujita<sup>6</sup>

<sup>1</sup>National Institute of Polar Research, Tokyo, Japan

<sup>2</sup>Meteorological Research Institute, Japan Meteorological Agency, Ibaraki, Japan

<sup>3</sup>Institute of Low Temperature Science, Hokkaido University, Hokkaido, Japan

<sup>4</sup>Avangnaq Arctic Project, Osaka, Japan

<sup>5</sup>Snow and Ice Research Center, National Research Institute for Earth Science and Disaster Resilience, Niigata, Japan

<sup>6</sup>Graduate School of Environmental Studies, Nagoya University, Nagoya, Japan

*Correspondence to:* Motoshi Nishimura (nishimura.motoshi@nipr.ac.jp)

**Abstract.** In situ meteorological data are essential to better understand ongoing environmental changes in the Arctic. Here, we present a dataset of quality-controlled meteorological observations by two automatic weather stations in northwest Greenland from July 2012 to the end of August 2020. The stations were installed in the accumulation area on the Greenland Ice Sheet (SIGMA-A site, 1490 m a.s.l.) and near the equilibrium line of the Qaanaaq Ice Cap (SIGMA-B site, 944 m a.s.l.). We describe the two-step sequence of quality-control procedures that we used to create increasingly reliable datasets by masking erroneous data records. Those data sets are archived in the Arctic Data archive System (ADS) (SIGMA-A; <http://doi.org/10.17592/001.2022041303>, SIGMA-B; <http://doi.org/10.17592/001.2022041306>). We analyzed the resulting 2012–2020 time series of air temperature, surface height, surface albedo, and histograms of longwave radiation (a proxy of cloudiness-formation-frequency). We found that surface height increased and no significant albedo decline in summer was observed albedo remained steady at the SIGMA-A site. In contrast, whereas high air temperatures and frequent clear-sky conditions in the summers of 2015, 2019, and 2020 at the SIGMA-B site caused prevailed while surface height was significantly albedo and surface lowering and albedo decreased in the summers of 2015, 2019, and 2020 at the SIGMA-B site. Therefore, it appears that these weather conditions difference, and it led to apparent surface height decrease at the SIGMA-B site but not at the SIGMA-A site. We anticipate that this quality-control method and these datasets will aid in climate studies of northwest Greenland as well as contribute to the advancement of broader polar climate studies.

## 33 1. Introduction

34 Automatic weather observation in Greenland started with GC-Net (Greenland Climate Network;  
35 Steffen and Box, 2001), which was established as a network of automatic weather stations (AWS) in  
36 Greenland after 1990. This observation network intended to provide long-term observations of  
37 climatological and glaciological factors over Greenland. This was followed by the PROMICE (van As  
38 et al., 2011; Fausto et al., 2021) led by the Geological Survey of Denmark and Greenland (GEUS) and  
39 the K-transect network (van de Wal et al., 2005), led by Utrecht University in the Netherlands, has  
40 been deployed. PROMICE is currently operating the largest observation network in Greenland by  
41 contracting the maintenance of GC-Net equipment, and K-transect has deployed equipment mainly in  
42 the western part of the country and continues to monitor the area closely. Both networks have provided  
43 important long-term meteorological data.

44 To contribute to these efforts and to fill a spatial gap, we established two AWS systems in northwest  
45 Greenland (Fig. 1), where rapid environmental changes have occurred in recent years (Aoki et al.,  
46 2014). Recent studies of this region have documented a drastic mass loss since the mid-2000s  
47 (Mouginot et al., 2019), an expansion of the ablation area (Noël et al., 2019), and a hot spot of  
48 increasing rainfall (Niwano et al., 2021). The two sites were established in 2012 as a part of the Snow  
49 Impurity and Glacial Microbe effects on abrupt warming in the Arctic (SIGMA) Project, which aimed  
50 to clarify the dramatic enhancement of melting of the Greenland Ice Sheet induced by snow impurities  
51 (e.g., black carbon, mineral dust). The observational data acquired since that time have been used by  
52 glaciological (Yamaguchi et al., 2014; Tsutaki et al., 2017; Matoba et al., 2018; Kurosaki et al., 2020),  
53 meteorological (Aoki et al., 2014; Tanikawa et al., 2014; Niwano et al., 2015; Hirose et al., 2021), and  
54 biological studies (Onuma et al., 2018; Takeuchi et al., 2018). These data are also valuable because  
55 they support the evaluation and development of numerical models (e.g., Niwano et al., 2018;  
56 Fujita et al., 2021) ~~and form the basis for robust analytical results.~~

57 The datasets from AWS generally contain erroneous data records that are attributed to natural  
58 factors (e.g., riming, ice accretion, snow accumulation on sensors) or technical issues (e.g., "Zero  
59 Offset"; (Behrens, 2021), faulty sensors) for radiation sensors. Various procedures exist for improving  
60 the quality of such datasets (e.g., Fiebrich et al., 2010; Fausto et al., 2021). In particular,  
61 careful Quality Control (QC) procedures, which is a process to improve the quality of data by  
62 removing outliers, are required for downward radiation sensors, which are sensitive to solar zenith  
63 angle, icing, riming, and snowfall (van den Broeke et al., 2004a, b; Moradi, 2009). Other QC  
64 procedures deal with error sources through range, step, and internal consistency tests (Estévez et al.,  
65 2011). The specifics of QC methods, for example, the threshold value for detecting erroneous data  
66 records, should be adjusted for each observation environment. In this paper, we describe the QC  
67 methods used for the in situ meteorological observation data from northwest Greenland, which include  
68 existing QC methods, new ones, and combinations of both.

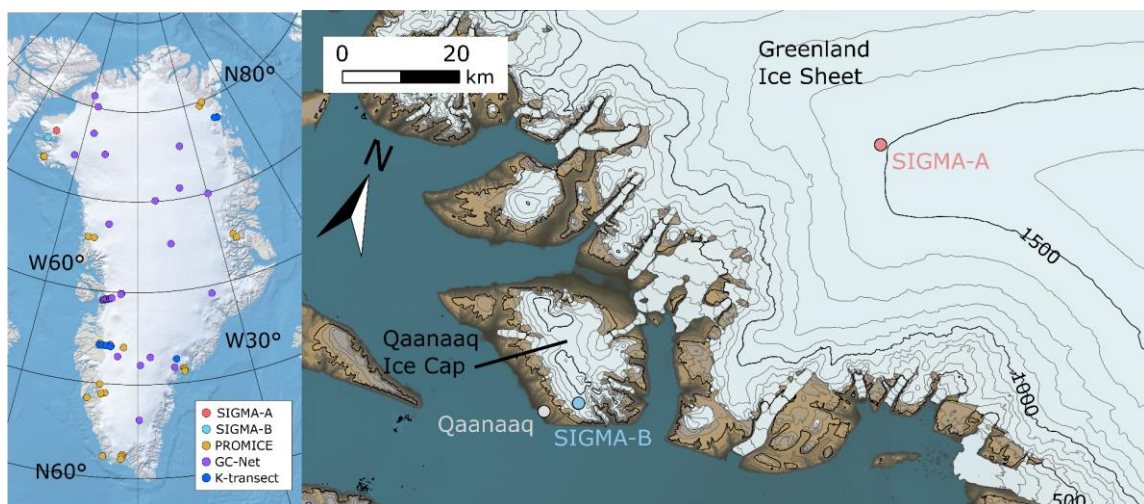
69 After describing the AWS sites (Sect. 2) and their datasets (Sect. 3), this paper introduces the two  
70 separate QC methods used sequentially to mask erroneous data records (Sect. 4). We then present  
71 examples of time series of meteorological variables in northwest Greenland, infer their implications  
72 for interannual variations in weather conditions, and describe the differences between the two sites  
73 (Sect. 5).

## 74 2. AWS general description

75 The two AWSs are installed at the SIGMA-A site ( $78.052^{\circ}$  N,  $67.628^{\circ}$  W; 1490 m a.s.l.), on the  
76 northwest Greenland Ice Sheet, and the SIGMA-B site ( $77.518^{\circ}$  N,  $69.062^{\circ}$  W; 944 m a.s.l.), on the  
77 Qaanaaq Ice Cap, a peripheral ice cap on the Greenland coast (Fig. 1). They have been in operation  
78 since July 2012 (Aoki et al., 2014). The observed parameters and these sensor specifications including  
79 abbreviations are listed in Table 1, and the other key constants, variables, and their abbreviations  
80 used in this study are also in Table 2.

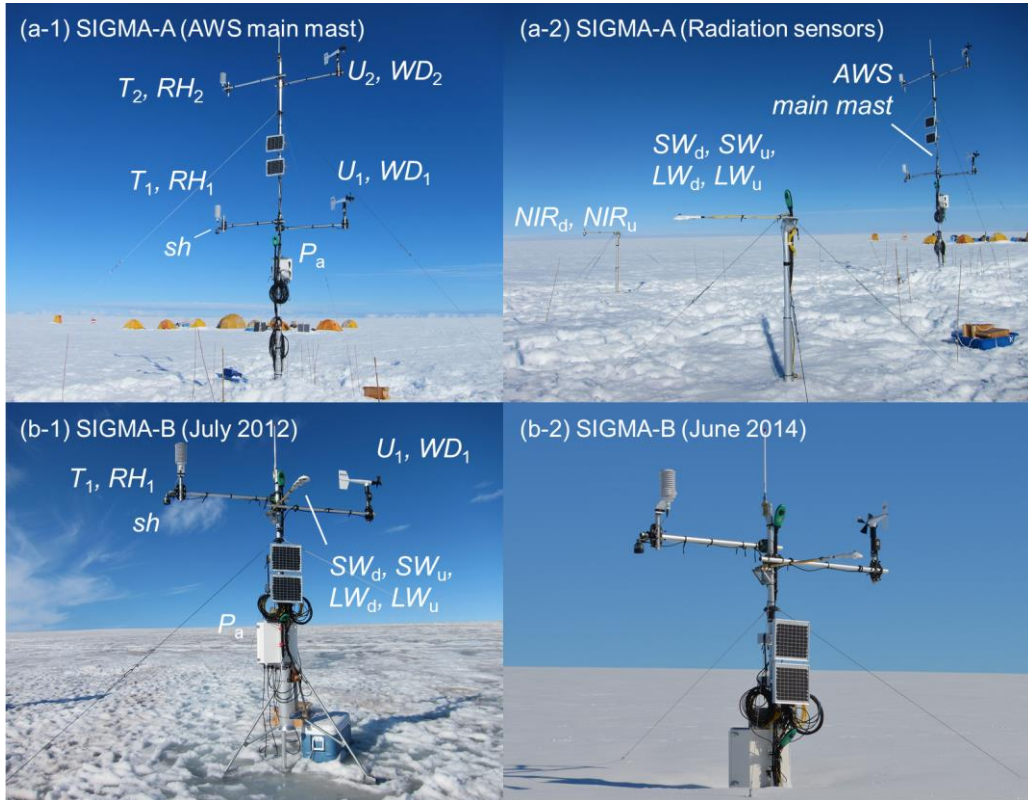
81 The SIGMA-A site is 70 km inland from the coast on a ridge of the Greenland Ice Sheet extending  
82 northwest from the Greenland Summit; it sits on a flat snow surface with no obstacles around the site  
83 (see Fig. 2). This site is in an accumulation area ~~offer~~ the ice sheet (Matoba et al., 2018) based on the  
84 analysis of ice-core data (Yamaguchi et al., 2014; Matoba et al., 2017). The SIGMA-B site is 3 km  
85 north of the village of Qaanaaq. This site is considered to be located ~~at~~ near the equilibrium line (910  
86 m a.s.l.; Tsutaki et al., 2017) on the Qaanaaq Ice Cap, which ranges in elevation between 30 and 1110  
87 m a.s.l. (Sugiyama et al., 2014). The surface condition at this site varies (see Fig. 2), and significant  
88 surface ~~lowering height-decreasing~~ has occurred in warm years (e.g., Aoki et al., 2014). The site is  
89 located on a southwest-facing slope (azimuth  $220^{\circ}$ ) with an angle of  $4^{\circ}$  according to 10 m DEM data  
90 (Porter et al., 2018).

91



92

93 Figure 1. Location map of Greenland showing PROMICE, GC-Net, and K-transect AWS sites (left)  
 94 and a local map of northwest Greenland showing locations of AWS sites SIGMA-A and SIGMA-B.  
 95 Contour interval in the right panel is 100 m.  
 96



97  
 98 Figure 2. Setting and instrumentation at the SIGMA-A site (top) and the SIGMA-B site (bottom).  
 99 Surface conditions at SIGMA-B are shown in July 2012 and June 2014. Sensors are labeled with the  
 100 observation parameters they measure (see Table 1).  
 101

102 Table 1. Meteorological observation parameters and sensor specifications.

observation parameter	abbreviation	unit	sensor	observation range	accuracy
wind speed	$U_n^a$	$\text{m s}^{-1}$	Young, 05103	0 to 100 [ $\text{m s}^{-1}$ ]	$\pm 0.3 \text{ m s}^{-1}$ or 1%
wind direction	$WD_n^a$	degree	Young, 05103	360° mechanical, 355° electrical (5° open)	$\pm 3^\circ$
air temperature	$T_n^a$	$^\circ\text{C}$	Vaisala, HMP155 <sup>b</sup>	-80 to +60 [ $^\circ\text{C}$ ]	$\pm 0.17 \text{ }^\circ\text{C}$
relative humidity <sup>c</sup>	$RH_n^a$	%	Vaisala, HMP155 <sup>b</sup>	0 to 100%	$\pm 1\%$ (0 to 90%) $\pm 1.7\%$ (90 to 100%)
atmospheric pressure	$P_a$	hPa	Vaisala, PTB210	500 to 1100 [hPa]	$\pm 0.30 \text{ hPa}$ at 20 $^\circ\text{C}$
downward and upward shortwave radiation	$SW_d, SW_u$	$\text{W m}^{-2}$	Kipp & Zonen, CNR4	0.3 to 2.8 [ $\mu\text{m}$ ]	$\pm 5\%$ (daily total)
downward and upward longwave radiation	$LW_d, LW_u$	$\text{W m}^{-2}$	Kipp & Zonen, CNR4	4.5 to 42 [ $\mu\text{m}$ ]	$\pm 10\%$ (daily total)
downward and upward near-infrared radiation	$NIR_d, NIR_u$	$\text{W m}^{-2}$	Kipp & Zonen, CMP6 with a RG715 cut-off filter	0.715 to 2.8 [ $\mu\text{m}$ ]	$\pm 5\%$ (daily total)
surface height	$sh$	cm	Campbell, SR50	0.5 to 10 [m]	1 cm or 0.4%
snow temperature	$st_n^a$	$^\circ\text{C}$	Climatec, C-PTWP-10	-40 to +60 [ $^\circ\text{C}$ ]	$\pm 0.15 \text{ }^\circ\text{C}$
tilts of the main mast	$Tilt_x, Tilt_y$	degree	TURCK, B2N85H-Q20L60-	-85° to +85°	$\pm 0.5^\circ$

a: "n" suffix is appended to distinguish the observation height or depth.  
 b: protected from direct solar irradiance by a naturally-aspirated 14-plate Gill radiation shield  
 c: Relative humidity is measured relative to water even in sub-freezing environments

103

105 Table 2. Key constants, variables, and their symbols used in this paper.

symbol	name	value	unit
constant			
$f_{nir}$	a fraction of near-infrared radiant flux in the shortwave radiant flux at the top of the atmosphere	0.5151	no dimension
$I_0$	solar constant	1361	$W m^{-2}$
$n$	cloud cover coefficient	0.5	no dimension
$r_m$	annual mean distance between the Sun and the Earth	$1.496 \times 10^8$	km
$sh_{initial}$	initial height of the surface height sensor	300	cm
$\alpha_{sw,max}$	maximum value of surface albedo	0.95	no dimension
$\alpha_{nir,max}$	maximum value of surface near-infrared albedo	0.90	no dimension
$\kappa$	constant depending on cloud type	0.26	no dimension
$\varepsilon$	snow/ice surface emissivity	0.98	no dimension
$\sigma$	Stefan-Boltzmann constant	$5.67 \times 10^8$	$W m^{-2} K^{-4}$
variable			
$d$	diffuse fraction in global radiation		no dimension
$I_d$	diffuse solar radiation		$W m^{-2}$
$I_s$	direct solar radiation		$W m^{-2}$
$LW_d$	downward longwave radiation		$W m^{-2}$
$LW_{std}$	standard atmospheric longwave radiation		$W m^{-2}$
$LW_u$	upward longwave radiation		$W m^{-2}$
$NIR_d$	downward near-infrared radiation		$W m^{-2}$
$NIR_u$	upward near-infrared radiation		$W m^{-2}$
$P_a$	atmospheric pressure		hPa
$r$	distance between the Sun and the Earth		m
$RH_{1,2}^a$	relative humidity		%
$sh$	surface height		cm
$sh_{raw}$	raw data of surface height		m
$solz$	solar zenith angle		degree
$solz_{slope}$	solar zenith angle for a slope		degree
$st_{1-6}^b$	snow temperature		$^{\circ}C$
$st_{depth_{1-6}}^b$	snow temperature sensor depth		m
$SW_d$	downward shortwave radiation		$W m^{-2}$
$SW_{d,slope}$	downward shortwave radiation for a slope		$W m^{-2}$
$SW_{TOA}$	downward shortwave radiation at the top of the atmosphere		$W m^{-2}$
$SW_u$	upward shortwave radiation		$W m^{-2}$
$t_r$	transmissivity of the atmosphere for shortwave radiation		no dimension
$T_{1,2}^a$	air temperature		$^{\circ}C$
$WD_{1,2}^a$	wind direction		degree
$U_{1,2}^a$	wind speed		$m s^{-1}$
$\alpha_{sw}$	surface albedo		no dimension
$\alpha_{sw,i}$	daily integrated surface albedo		no dimension
$\alpha_{nir}$	surface near-infrared albedo		no dimension
$\alpha_{nir,i}$	daily integrated surface near-infrared albedo		no dimension
$\beta$	slope angle		radian
$\varepsilon_0$	clear-sky atmospheric emissivity		no dimension
$\varepsilon^*$	atmospheric emissivity		no dimension
$\theta$	solar zenith angle		radian
$\theta_{slope}$	solar zenith angle for a slope		radian
$\phi$	solar azimuth angle		radian
$\phi_{slope}$	solar azimuth angle of a slope		radian

<sup>a</sup> 1: observed at lower height, 2: observed at upper height (only at the SIGMA-A site)

<sup>b</sup> 1-6: observing depth

symbol	name	value	unit
constant			
$f_{nir}$	a fraction of near-infrared radiant flux in the shortwave radiant flux at the top of the atmosphere	0.5151	no dimension
$I_0$	solar constant	1361	$W m^{-2}$
$n$	cloud cover coefficient	0.5	no dimension
$r_m$	annual mean distance between the Sun and the Earth	$1.496 \times 10^8$	km
$sh_{initial}$	initial height of the surface height sensor	300	cm
$\alpha_{sw,max}$	maximum value of surface albedo	0.95	no dimension
$\alpha_{nir,max}$	maximum value of surface near-infrared albedo	0.90	no dimension
$\kappa$	constant depending on cloud type	0.26	no dimension
$\varepsilon$	snow/ice surface emissivity	0.98	no dimension
$\sigma$	Stefan-Boltzmann constant	$5.67 \times 10^8$	$W m^{-2} K^{-4}$
variable			
$d$	diffuse fraction in global radiation		no dimension
$I_d$	diffuse solar radiation		$W m^{-2}$
$I_s$	direct solar radiation		$W m^{-2}$
$LW_d$	downward longwave radiation		$W m^{-2}$
$LW_{std}$	standard atmospheric longwave radiation		$W m^{-2}$
$LW_u$	upward longwave radiation		$W m^{-2}$
$NIR_d$	downward near-infrared radiation		$W m^{-2}$
$NIR_u$	upward near-infrared radiation		$W m^{-2}$
$P_a$	atmospheric pressure		hPa
$r$	distance between the Sun and the Earth		m
$RH_{1,2}^a$	relative humidity		%
$sh$	surface height		cm
$sh_{raw}$	raw data of surface height		m
$solz$	solar zenith angle		degree
$solz_{slope}$	solar zenith angle for a slope		degree
$st_{1-6}^b$	snow temperature		$^{\circ}C$
$st_{depth_{1-6}}^b$	snow temperature sensor depth		cm
$SW_d$	downward shortwave radiation		$W m^{-2}$
$SW_{d,slope}$	downward shortwave radiation for a slope		$W m^{-2}$
$SW_{TOA}$	downward shortwave radiation at the top of the atmosphere		$W m^{-2}$
$SW_u$	upward shortwave radiation		$W m^{-2}$
$t_r$	transmissivity of the atmosphere for shortwave radiation		no dimension
$T_{1,2}^a$	air temperature		$^{\circ}C$
$WD_{1,2}^a$	wind direction		degree
$U_{1,2}^a$	wind speed		$m s^{-1}$
$\alpha_{sw}$	surface albedo		no dimension
$\alpha_{sw,i}$	daily integrated surface albedo		no dimension
$\alpha_{nir}$	surface near-infrared albedo		no dimension
$\alpha_{nir,i}$	daily integrated surface near-infrared albedo		no dimension
$\beta$	slope angle		radian
$\varepsilon_0$	clear-sky atmospheric emissivity		no dimension
$\varepsilon^*$	atmospheric emissivity		no dimension
$\theta$	solar zenith angle		radian
$\theta_{slope}$	solar zenith angle for a slope		radian
$\phi$	solar azimuth angle		radian
$\phi_{slope}$	solar azimuth angle of a slope		radian

<sup>a</sup> 1: observed at lower height, 2: observed at upper height (only at the SIGMA-A site)

<sup>b</sup> 1-6: observing depth

### 109 3. Description of AWS systems and datasets

#### 110 3.1. Specifications

111 Each AWS main mast is set in a hole drilled using a hand auger. Sensors for air temperature,  
112 relative humidity, and wind speed and direction are mounted at the ends of horizontal poles to exclude  
113 possible thermal and wind disturbances from the main mast. The SIGMA-A sensors are placed 3 m  
114 and 6 m above the surface, as signified by subscripts “1” (lower) and “2” (upper) in the corresponding  
115 data variables. The SIGMA-B sensors are set at 3 m above the surface and have subscripts of “1”. The  
116 surface height sensor at both sites is mounted at 3 m height beneath the air temperature and relative  
117 humidity sensors. Six snow temperature sensors have been set as follows. Four sensors were set at  
118 19:00 UTC on 29 June 2012 at depths of 100 cm ( $st_1$ ), 70 cm ( $st_2$ ), 40 cm ( $st_3$ ), and 5 cm ( $st_4$ )  
119 ~~below~~ under the snow surface. At 21:00 UTC on 27 July 2013, sensors  $st_3$  and  $st_4$  were relocated to  
120 depths of 46 cm and 16 cm, respectively. Sensors  $st_5$  and  $st_6$  were set at 5 cm under the surface and 45  
121 cm above the surface, respectively, at 14:00 UTC on 9 June 2014. Sensors for shortwave, longwave,  
122 and near-infrared radiation are installed at SIGMA-A on separate poles 10 m from the main mast (Fig.  
123 2a-2). A pyranometer and a pyrgeometer at SIGMA-B are mounted on the main mast facing directly  
124 south. Tilt angles of the main mast in the north-south ( $Tilt_x$ ) and east-west ( $Tilt_y$ ) directions are  
125 monitored with an inclinometer attached to the main mast. The additional suffix “A” or “B” represents  
126 the site name in the variables introduced below.

127 Electric power is supplied to the AWS systems by a lead-acid battery that is charged constantly by  
128 solar panels attached to the main mast. All parameters are recorded once per minute and stored in a  
129 data logger (C-CR1000, Campbell Scientific, USA), except for the main mast’s surface height and tilt  
130 angles, which are recorded every hour. Hourly data are calculated for the other parameters by  
131 averaging the 1-min data. All hourly data are sent regularly to the data server via the Argos satellite  
132 channel.

133 Surface height is measured with an ultrasonic snow gauge (Table 1). The raw data from this sensor  
134 ( $sh_{raw}$ ) is the distance from the sensor to the snow surface, which has a temperature dependence. The  
135 temperature-corrected surface height ( $sh$ ) is calculated from

$$136 \quad sh = sh_{initial} - sh_{raw} \times \sqrt{\frac{T_2 + 273.15}{273.15}} \times 100, \quad (i)$$

137 where  $sh_{initial}$  (= 300 cm) is the initially installed sensor height from the surface and  $T_2$  is air  
138 temperature.

139

#### 140 3.2. Data processing

141 We describe the calculations for some variables used in the QC process in this section. To

142 accurately calculate the surface albedo and surface energy balance at the SIGMA-B site, we considered  
 143 the impact of the sloping surface on the vertical radiant flux. To account for this effect, we derived the  
 144 slope-corrected downward shortwave radiation ( $SW_{d\_slope}$ ) using the methods in Jonsell et al. (2003)  
 145 and Hock and Holmgren (2005). The  $SW_{d\_slope}$  is calculated by

$$146 \quad SW_{d\_slope} = I_s + I_d, \quad (ii)$$

147 where  $I_s$  and  $I_d$  are the direct and diffuse shortwave radiation for a slope, respectively:

$$148 \quad I_s = SW_d \times d, \quad (iii)$$

$$149 \quad I_d = SW_d \times (1 - d) \times \frac{\cos \theta_{slope}}{\cos \theta}, \quad (iv)$$

150 where  $d$  is the ratio of total diffuse radiation to global radiation and  $\theta$  and  $\theta_{slope}$  [radian] are the solar  
 151 zenith angle and the solar zenith angle for a slope, respectively. The ratio  $d$  is obtained from  
 152 atmospheric transmittance  $t_r$  by

$$153 \quad d = \begin{cases} 0.15 & \text{for } 0.8 \leq t_r, \\ 0.929 + 1.134t_r - 5.111t_r^2 + 3.106t_r^3 & \text{for } 0.15 < t_r < 0.8, \\ 1.0 & \text{for } t_r \leq 0.15, \end{cases} \quad (v)$$

154 where

$$155 \quad t_r = \frac{SW_d}{SW_{TOA}}, \quad (vi)$$

156 where  $SW_{TOA}$  is the downward shortwave radiation at the top of the atmosphere, calculated by

$$157 \quad SW_{TOA} = I_0 \left( \frac{r_m}{r} \right)^2 \cos \theta, \quad (vii)$$

158 where  $I_0$  ( $= 1361 \text{ W m}^{-2}$ ) is the solar constant (Rottman, 2006; Fröhlich, 2012),  $r$  is the distance  
 159 between the Sun and the Earth (assuming an elliptical orbit with an eccentricity of 0.01637), and  $r_m$  is  
 160 its annual mean ( $= 1.496 \times 10^8 \text{ km}$ ).

161 The solar zenith angle for a slope in Eq. (iv) is calculated by

$$162 \quad \cos \theta_{slope} = \cos \beta \cos \theta + \sin \beta \sin \theta \cos(\varphi - \varphi_{slope}), \quad (viii)$$

163 where  $\beta$  is the slope angle from a horizontal plane, and  $\varphi$  and  $\varphi_{slope}$  are the solar azimuth and the solar  
 164 azimuth for the slope direction, respectively. Solar zenith and azimuth angles are calculated from the  
 165 geographic position of the observation site and the date and time.

166 Shortwave and near-infrared albedos ( $a_{sw}$  and  $a_{nir}$ , respectively) are calculated as the ratio of  
 167 upward and downward radiant fluxes, as shown for  $a_{sw}$  by

$$168 \quad \alpha_{sw} = \frac{SW_u}{SW_d}, \quad (ix)$$

169 where  $SW_u$  is the upward shortwave radiant flux and  $SW_d$  is the downward shortwave radiant flux.  
 170  $SW_{d\_slope}$  is used for  $SW_d$  when calculating  $a_{sw}$  at the SIGMA-B site. The daily integrated shortwave  
 171 albedo ( $a_{sw,i}$ ) is calculated as the ratio of cumulative upward and downward radiant fluxes for the past



172 24 h:

$$173 \quad \alpha_{sw,i} = \sum_{24h} SW_u / \sum_{24h} SW_d. \quad (x)$$

174 The near-infrared albedo ( $a_{nir}$ ) and daily integrated near-infrared albedo ( $a_{nir,i}$ ) are calculated in the  
175 same way. The near-infrared fraction is the ratio of the downward near-infrared radiant flux ( $NIR_d$ ) to  
176  $SW_d$ .

177 Note that some parameters may require correction or caution depending on the observation  
178 environment. First, since temperature and humidity shelters are naturally ventilated, air temperature  
179 value may have a positive bias due to shelter heating from solar radiation (e.g., Morino et al, 2021).  
180 In addition, in sub-freezing conditions, relative humidity may not be measured correctly because the  
181 sensor used in this study (Vaisala, HMP155) calculates relative humidity as liquid water vapor pressure  
182 even in sub-freezing environments and whenif the shelter is covered by rime or frost (Makkonen and  
183 Laakso, 2005). Aoki et al. (2011) pointed out that the pole on which the radiometer is mounted casts  
184 a shadow on the radiation sensor. In addition, reflected and shielding scattered radiations due to the  
185 AWS including solar panels which may result in incorrect radiation measurements, although no  
186 anomalous radiation data due to these factors were found. Although the possibility of data correction  
187 as described above is recognized, the focus of this paper is to open the observed values themselves,  
188 without any correction or data processing that might involve the implementer's intention. Therefore,  
189 we will note only the correction possibilities and present the observed data in this study.

#### 190 4. Quality control

191 The datasets of observations at sites SIGMA-A and SIGMA-B are classified into four QC levels  
192 numbered 1.0 to 1.3. A Level 1.0 dataset, which is not archived in any repository, is a raw dataset  
193 without data processing. A Level 1.1 dataset is a raw dataset with flags added to indicate missing data  
194 for periods when the data logger was inoperative. A Level 1.2 dataset has undergone an initial control,  
195 which uses a simple masking algorithm to eliminate anomalous values that violate physical laws or  
196 are impossible in the observed environment. The initial control improves the accuracy of the statistical  
197 processing that follows and reduces the possibility of excluding true values. A Level 1.3 dataset has  
198 undergone a secondary control, in which statistical methods are used on Level 1.2 data to identify and  
199 mask outlier values. It has also undergone a final manual masking procedure, in which a researcher  
200 visually checks the dataset and masks outliers based on subjective criteria.

201 The initial control method is described in Sect. 4.1 and the secondary control method is described  
202 in Sect. 4.2. In these sections, the parameter suffixes related to the differences in observation height  
203 (1 and 2) and sites (A and B) are omitted except when needed for clarity, and subscripts indicating  
204 upward and downward radiation (d; downward, u; upward) is denoted as  $\chi$  in the equation. Erroneous  
205 records are flagged with one of the following numerical expressions to signify the reason they have

206 been flagged:  
207 –9999: a missing or erroneous data record attributed to a mechanical malfunction or a local  
208 phenomenon such as sensor icing, riming, or burial in snow.  
209 –9998: an erroneous radiation record when the radiant sensor was covered with snow or frost.  
210 –9997: a record of snow temperature sensor depth when the sensor was suspected to be located above,  
211 not below the snow surface.  
212 –8888: a record flagged during the manual masking procedure.

#### 213 4.1. Initial QC for Level 1.2 datasets

214 The objectives of the initial control are to eliminate erroneous records due to mechanical  
215 malfunctions or local phenomena and pre-treat Level 1.1 datasets for the secondary control. The initial  
216 control consists of a range test (e.g., Fiebrich et al., 2010; Estévez et al., 2011) and a manual mask  
217 procedure. The range test sets variation ranges (see Tables 3 and 4) for each observed parameter in  
218 northwest Greenland on the basis of simple statistics ~~based on (maximum, minimum, and mean values)~~  
219 derived from records in the Level 1.1 dataset during a period with no obvious erroneous data. Records  
220 outside this statistical range are flagged with a “–9999” code. Tables 3 and 4 list the parameters  
221 subjected to this test and their assigned ranges. The manual masking procedure identified specific  
222 erroneous values that resulted from an electrical malfunction and flagged them with a “–8888” code.  
223 The following subsections offer detailed and additional explanations of the initial control, however,  
224 ~~the range test for each parameter is listed in Table 3, in the detail description of it for each parameter~~  
225 ~~is omitted in the following sections description, only the procedure numbers in Table 3 are referenced~~  
226 ~~as necessary, and the explanation of the range test is omitted.~~

##### 227 4.1.1. Wind speed and wind direction

228  $U_{\max}$  used in the range test is the maximum value between the beginning of observation and 31  
229 August 2020, and  $+15.0 \text{ m s}^{-1}$  was taken as the range margin for the upper limit of  $U_n$ . In addition to  
230 the range test, the following basic processing was also performed. When  $U_n$  was zero (no wind),  $WD_n$   
231 was flagged as erroneous:

$$232 \quad U_n = 0 \text{ and } WD_n > 0 \rightarrow WD_n \text{ flagged } -9999. \quad (1.1.1)$$

233 When  $WD_n$  had a negative value, it was flagged as erroneous:

$$234 \quad WD_n \leq 0 \rightarrow WD_n \text{ flagged } -9999. \quad (1.1.2)$$

##### 235 4.1.2. Air temperature and relative humidity

236  $T_{n_{\max}}$  and  $T_{n_{\min}}$  were determined from the entire observation period ~~ending 31 August 2020~~. The  
237 range margin for  $T_n$  was set as  $\pm 10.0 \text{ }^\circ\text{C}$ . Discrepancies arising from the dual sensors at SIGMA-A

238 were addressed in the secondary control (see Sect. 4.2.2).

### 239 4.1.3. Shortwave and near-infrared radiation

240 The main objective of the initial control for shortwave radiation was to mask erroneous records  
241 attributed to Zero Offset (Behrens, 2021). Zero Offset is a few watts of radiation that occurs at night  
242 caused by the slight temperature difference between the two detectors (inside of the dome shelter and  
243 sensor body). However, since the value is an observation error, the observed value may be different  
244 from the original radiation balance and need to be masked.

245 The range test is based on the assumption that  $SW_d$  cannot exceed the maximum of  $SW_{TOA}$   
246 ( $SW_{TOA\_max}$ ) during the observation period ( $761.6 \text{ W m}^{-2}$  at SIGMA-A and  $772.2 \text{ W m}^{-2}$  at SIGMA-  
247 B), and albedos  $a_{sw}$  and  $a_{nir}$  cannot be higher than  $a_{sw\_max}$  and  $a_{nir\_max}$  ( $a_{sw\_max} = 0.95$  and  $a_{nir\_max} =$   
248  $0.90$ ), respectively, as determined from the radiative transfer model calculation (Aoki et al., 2003).  
249 Moreover, the fraction of the near-infrared spectral domain at the top of the atmosphere ( $f_{nir}$ ) is  
250 assumed to be equal to 0.5151 based on the extraterrestrial spectral solar radiation (Wehrli, 1985).  
251 Based on those assumptions, upward and downward radiation fluxes were flagged as erroneous  
252 according to the range tests in Table 3.

253 The following procedures were also applied to mask erroneous records due to Zero Offset. These  
254 parameters were flagged as erroneous (-9999) in a following case (using  $SW_\chi$  as an example):

$$255 \quad SW_\chi < 0 \text{ and } solz < 90.0 \rightarrow SW_\chi \text{ flagged } -9999, \quad (1.3.1)$$

$$256 \quad SW_\chi < 0 \text{ and } solz \geq 90.0 \rightarrow SW_\chi = 0. \quad (1.3.2)$$

### 257 4.1.4. Longwave radiation

258 The range tests were performed for  $LW_d$  and  $LW_u$  under the conditions in Table 3.  $LW_{d\_max}$  and  
259  $LW_{u\_max}$  were determined as follows:

$$260 \quad LW_{d\_max} = \varepsilon_{max} \sigma T_{max}, \quad (1.4.1)$$

$$261 \quad LW_{u\_max} = \varepsilon \sigma T_{s\_max}. \quad (1.4.2)$$

262 However,  $T_{max}$  is  $T_{2A\_max}$  for the SIGMA-A site and  $T_{1B\_max}$  for the SIGMA-B site. Maximum values  
263 were determined under the following assumptions: (1)  $T_{2A}$  and  $T_{1B}$  cannot be larger than  $T_{2A\_max}$  and  
264  $T_{1B\_max}$ , respectively, (2) atmospheric emissivity is set to unity ( $\varepsilon_{max}$ ), and (3) the value of  $LW_{u\_max}$  is  
265 determined as the amount of radiation corresponding to longwave emission at  $T_{s\_max}$  ( $= 10 \text{ }^\circ\text{C}$ ), which  
266 includes errors due to longwave emissions from the poles of the AWS system and similar sources, and  
267 that the emissivity of the snow/ice surface ( $\varepsilon$ ) is 0.98 (Armstrong and Brun, 2008).

268 Both upward and downward longwave fluxes were considered erroneous when the sensor appeared  
269 to be covered with snow or frost:

$$270 \quad |LW_d - LW_u| \leq 1.0 \rightarrow LW_d \text{ and } LW_u \text{ flagged } -9998. \quad (1.4.3)$$

271 **4.1.5. Surface height**

272 The range test for surface height ( $sh$ ) was imposed separately for each period between  
 273 maintenances to the SIGMA-A site, when the main mast extension was adjusted to prevent the sensors  
 274 from being buried in snow. (A single range test sufficed for SIGMA-B.) For each test, the range was  
 275 set so that  $sh$  varied from the median by  $\pm 100$  cm or  $\pm 150$  cm, a margin that was determined depending  
 276 on the variation of the data records in each period. The objective of this range test (Procedure 1.5.1;  
 277 Table 3) was to mask the most obvious outliers. In addition, corrections were made to the  $sh$  records  
 278 after each of three maintenance visits to the AWS at SIGMA-A.

279 **4.1.6. Atmospheric pressure**

280  $P_{a\_ave}$  used in the range test is the average atmospheric pressure for the observation period at each  
 281 AWS site (Table 3). The additional margin that defined the range was  $\pm 100$  hPa.

282 **4.1.7. Snow temperature**

283 The range test for snow temperature was conducted using following threshold values;  $T_{1\_min}$  is  
 284 the minimum air temperature for the site and the upper threshold,  $0.2$  °C, incorporates the sensor's  
 285 absolute error of  $0.15$  °C and the requirement that the snow temperature cannot be positive.

286  
 287 Table 3. Range test coverage for each parameter used in the QC procedures. The variable subscripts  
 288 “n” (1 or 2) and  $\chi$  indicate the distinction of sensors height and the direction of radiation flux (upward  
 289 or downward), respectively.

parameter	variable	unit	range test		procedure No.
			value	range	
wind speed	$U_1, U_2$	$m\ s^{-1}$	$0 <$	$U_n < U_{max} + 15.0$	1.1.3
wind direction <sup>a</sup>	$WD_1, WD_2$	degree	$0 <$	$WD_n \leq 360$	1.1.4
air temperature	$T_1, T_2$	°C	$T_{n,min} - 10.0 <$	$T_n < T_{n,max} + 10.0$	1.2.1
relative humidity	$RH_1, RH_2$	%	$0 \equiv$	$RH_n \leq 100$	1.2.2
shortwave radiation	$SW_d, SW_u$	$W\ m^{-2}$	$SW_d < SW_{TOA,max}$		1.3.3
			$SW_u < SW_{TOA,max} \times a_{sw,max}$		1.3.5
			$SW_d < T_{IA}\ (or\ B) \times SW_{TOA,max}$		2.3.2
near-infrared radiation <sup>b</sup>	$NIR_d, NIR_u$	$W\ m^{-2}$	$NIR_d < f_{nir} \times SW_{TOA,max}$		1.3.4
			$NIR_u < f_{nir} \times SW_{TOA,max} \times a_{nir,max}$		1.3.6
			$NIR_d < T_{IA} \times f_{nir} \times SW_{TOA,max}$		2.3.3
surface albedo	$a_{sw}$	-	$0.6 < a_{sw} < 0.95$ (for October–April in SIGMA-A)		2.4.1
			$0.4 < a_{sw} < 0.95$ (for May–September in SIGMA-A)		2.4.2
			$0.4 < a_{sw} < 0.95$ (for October–April in SIGMA-B)		2.4.3
			$0.1 < a_{sw} < 0.95$ (for May–September in SIGMA-B)		2.4.4
surface near-infrared albedo	$a_{nir}$	-	$0.5 < a_{nir} < 0.90$ (for October–April in SIGMA-A)		2.4.5
			$0.3 < a_{nir} < 0.90$ (for May–September in SIGMA-A)		2.4.6
longwave radiation	$LW_d, LW_u$	$W\ m^{-2}$	$0 <$	$LW_\chi < LW_{\chi,max}$	1.4.4
surface height	$sh$	cm	$median\_sh - 100.0$ or $150.0^c <$	$sh < median\_sh + 100.0$ or $150.0^c$	1.5.1
atmospheric pressure	$P_a$	hPa	$P_{a,ave} - 100.0 <$	$P_a < P_{a,ave} + 100.0$	1.6.1
snow temperature <sup>b</sup>	$st$	°C	$T_{1,min} - 10.0 <$	$st_n < 0.2$	1.7.1

<sup>a</sup> in case of  $U_n > 0$

<sup>b</sup> only SIGMA-A site

<sup>c</sup> the margin is changed depending on a variation of the data record in each applied period.

290

291

292 Table 4. Statistical Threshold values used in the range tests, determined from the entire observation  
 293 period up to 31 August 2020.

meteorological parameter	unit	threshold value			
		SIGMA-A		SIGMA-B	
		parameter name	value	parameter name	value
wind speed	$\text{m s}^{-1}$	$U_{1A\_max}$	23.9	$U_{1B\_max}$	21.9
		$U_{2A\_max}$	25.5	–	–
air temperature	$^{\circ}\text{C}$	$T_{1A\_max}$	7.2	$T_{1B\_max}$	10.7
		$T_{2A\_max}$	7.2	–	–
		$T_{1A\_min}$	–49.9	$T_{1B\_min}$	–40.5
		$T_{2A\_min}$	–49.9	–	–
longwave radiation	$\text{W m}^{-2}$	$LW_{dA\_max}$	418.8	$LW_{dB\_max}$	440.1
		$LW_{uA\_max}$	357.2	$LW_{uB\_max}$	357.2
atmospheric pressure	hPa	$P_{a\_aveA}$	833.1	$P_{a\_aveB}$	894.2

294

295

296 **4.2. Secondary QC for Level 1.3 datasets**

297 The secondary control applies another range test, an anomaly test, and a manual mask procedure.  
 298 The range test sets a more precise variation range than the initial control and masks erroneous data  
 299 records. The anomaly test sets a median and standard deviation (SD), which govern statistical tests as  
 300 follows;

301 
$$\beta < \text{median}_\beta + \text{SD}_\beta \times \gamma, \tag{2.0.1}$$

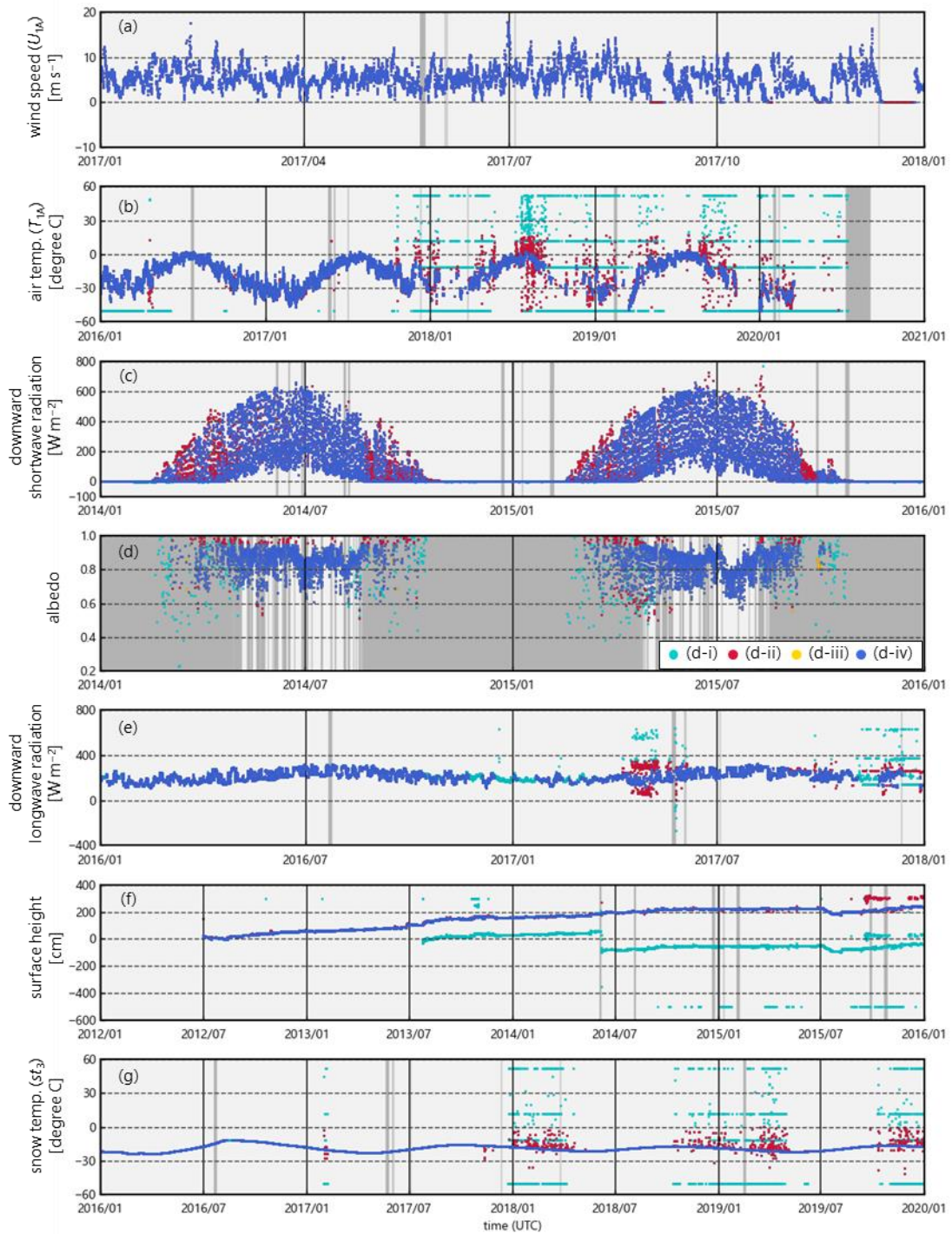
302 where  $\beta$  is an arbitrary variable and the multiplier  $\gamma$  is 1, 2, or 3 depending on the intensity of the  
 303 anomaly variation, and determined based on the test results in each case. Those statistical values and  
 304 the multiplier can be referred in the QC program. This study determined the possible range of  
 305 correctnormal values in the Level 1.2 dataset and identify and mask outliers if the variable deviates  
 306 from its normal range. The manual mask procedure identifies and masks any remaining erroneous  
 307 records. As a result of data masking by the initial control and the secondary control, the percentage of  
 308 unmasked records for each parameter at three data levels is shown in Table 5, and the effects of the  
 309 two controls are illustrated in Fig. 3 and described in detail below.

310

311 Table 5. Percentage of unmasked data for each parameter in each dataset.

	SIGMA-A			SIGMA-B		
	Level 1.1	Level 1.2	Level 1.3	Level 1.1	Level 1.2	Level 1.3
	%	%	%	%	%	%
$U_1$	98.0	98.0	92.1	99.7	99.7	97.7
$WD_1$	98.0	96.7	91.8	99.7	99.2	97.2
$T_1$	98.0	73.4	68.4	99.7	99.7	99.7
$RH_1$	98.0	50.7	43.6	99.7	99.7	98.8
$U_2$	98.0	98.0	94.1	-	-	-
$WD_2$	98.0	97.1	93.8	-	-	-
$T_2$	98.0	98.0	97.8	-	-	-
$RH_2$	98.0	98.0	98.0	-	-	-
$SW_d$	98.0	97.9	86.2	99.7	99.5	85.2
$SW_u$	98.0	97.9	98.1	99.7	99.7	99.7
$LW_d$	98.0	75.3	68.9	99.7	91.0	91.0
$LW_u$	98.0	68.7	67.4	99.7	91.0	91.0
$NIR_d$	98.0	97.9	86.6	-	-	-
$NIR_u$	98.0	97.9	98.0	-	-	-
$sh$	98.0	85.5	75.8	99.7	90.2	87.1
$P_a$	98.0	97.9	97.9	99.7	99.7	99.7
$st_1$	98.0	97.6	96.7	-	-	-
$st_2$	98.0	97.9	97.3	-	-	-
$st_3$	98.0	88.8	87.2	-	-	-
$st_4$	98.0	97.0	96.2	-	-	-
$st_5$	98.0	94.9	72.3	-	-	-
$st_6$	98.0	95.2	56.7	-	-	-
$a_{sw}$	-	-	31.6	-	-	32.4
$a_{nir}$	-	-	33.5	-	-	-
$st\_depth_1$	-	-	75.8	-	-	-
$st\_depth_2$	-	-	75.8	-	-	-
$st\_depth_3$	-	-	75.8	-	-	-
$st\_depth_4$	-	-	75.8	-	-	-
$st\_depth_5$	-	-	52.7	-	-	-
$st\_depth_6$	-	-	36.9	-	-	-
$SW_{d\_slope}$	-	-	-	-	-	83.7

	SIGMA-A			SIGMA-B		
	Level 1.1	Level 1.2	Level 1.3	Level 1.1	Level 1.2	Level 1.3
	%	%	%	%	%	%
$U_1$	98.0	98.0	92.1	99.7	99.7	97.7
$WD_1$	98.0	96.7	91.8	99.7	99.2	97.2
$T_1$	98.0	73.4	68.4	99.7	99.7	99.7
$RH_1$	98.0	50.7	43.6	99.7	99.7	98.8
$U_2$	98.0	98.0	94.1	–	–	–
$WD_2$	98.0	97.1	93.8	–	–	–
$T_2$	98.0	98.0	97.8	–	–	–
$RH_2$	98.0	98.0	98.0	–	–	–
$SW_d$	98.0	97.9	86.0	99.7	99.5	85.2
$SW_u$	98.0	97.9	97.8	99.7	99.7	99.7
$LW_d$	98.0	75.3	68.9	99.7	91.0	91.0
$LW_u$	98.0	68.7	67.4	99.7	91.0	91.0
$NIR_d$	98.0	97.9	86.4	–	–	–
$NIR_u$	98.0	97.9	97.8	–	–	–
$sh$	98.0	85.5	75.8	99.7	90.2	87.1
$P_a$	98.0	97.9	97.9	99.7	99.7	99.7
$st_1$	98.0	97.6	96.7	–	–	–
$st_2$	98.0	97.9	97.3	–	–	–
$st_3$	98.0	88.8	87.2	–	–	–
$st_4$	98.0	97.0	96.2	–	–	–
$st_5$	98.0	94.9	72.3	–	–	–
$st_6$	98.0	95.2	56.7	–	–	–
$a_{sw}$	–	–	31.6	–	–	32.4
$a_{nir}$	–	–	33.5	–	–	–
$st\_depth_1$	–	–	75.8	–	–	–
$st\_depth_2$	–	–	75.8	–	–	–
$st\_depth_3$	–	–	75.8	–	–	–
$st\_depth_4$	–	–	75.8	–	–	–
$st\_depth_5$	–	–	52.7	–	–	–
$st\_depth_6$	–	–	36.9	–	–	–
$SW_{d\_slope}$	–	–	–	–	–	83.7



314

315 Figure 3. Examples of the initial and secondary controls for the SIGMA-A site: (a) wind speed ( $U_{1A}$ ),  
 316 (b) air temperature ( $T_{1A}$ ), (c) downward shortwave radiation, (d) surface albedo, (e) downward  
 317 longwave radiation, (f) surface height, and (g) snow temperature ( $st_3$ ). In all panels except (d), the dark  
 318 gray areas represent time periods in which data records in the Level 1.0 dataset were masked to  
 319 produce the Level 1.1 dataset, light blue dots denote records masked by the initial control, red dots



320 denote records masked by the secondary control, and dark blue dots are the Level 1.3 data records. In  
321 panel (d), the gray shaded area represents the masked (–9999) data records that cannot be calculated  
322 due to the absence of, masked  $SW_d$ , or for other reasons. The light blue, red and yellow dots represent  
323 data points masked by three QC operations during the secondary control; see Sect. 4.2.4 for  
324 explanation.

#### 325 4.2.1. Wind speed and wind direction

326 When  $U_n$  was zero for more than 6 continuous hours,  $U_n$  and  $WD_n$  were both flagged as erroneous  
327 (–9999) under the assumption that the wind sensor was blocked by snow and ice. Although the initial  
328 control eliminated no  $U_n$  records, this step masked many values in the winter (Fig. 3a).

#### 329 4.2.2. Air temperature and relative humidity

330 Anomaly tests for air temperature and relative humidity were only applied to the lower-level sensor  
331 records for SIGMA-A (i.e.,  $T_{1A}$  and  $RH_{1A}$ ). The anomaly test compared the difference ( $\Delta T$  and  $\Delta RH$ )  
332 between readings of the upper and lower sensors (i.e.,  $|T_{1A} - T_{2A}|$  and  $|RH_{1A} - RH_{2A}|$ ) to the  
333 respective medians and SDs of those parameters. The medians were calculated from the data before 1  
334 September 2017, because the data after that date appeared to include many erroneous  $T_{1A}$  records due  
335 to deterioration of the data logger or sensor. The SD criterion ( $\gamma$  in Procedure 2.0.1) was adjusted  
336 modestly ( $\gamma = 3$ ) before 1 September, 2017 and more stringently ( $\gamma = 1$ ) to detect outliers in the records  
337 of  $T_{1A}$  and  $RH_{1A}$  after the date, which were flagged as erroneous (–9999). The effectiveness of this  
338 adjustment is ~~shown~~ in Fig. 3b.

#### 339 4.2.3. Shortwave and near-infrared radiation

340 The anomaly test for shortwave and near-infrared radiation was intended to mask the noise  
341 resulting from a weak electric pulse at large solar zenith angles. The median and SD values were  
342 calculated only from ~~only~~ the records ( $SW_d$ ,  $SW_u$ ,  $NIR_d$ , and  $NIR_u$ ) at  $solz > 90.0^\circ$  to distinguish this  
343 noise source according to Procedure 2.0.1 for above parameters, where  $\gamma = 3$ . If the record is in ~~is in~~  
344 ~~from~~ its anomaly range, the records were identified as noise and modified to zero.

345 The downward radiation components were sometimes overestimated as a result of icing or riming  
346 over the glass dome of the pyranometer. To mask these erroneous values, we applied range tests based  
347 on  $SW_{TOA}$  and threshold values of atmospheric transmittance for each site  $T_{rA}$  and  $T_{rB}$  ( $T_{rA} = 0.881$   
348 and  $T_{rB} = 0.872$ ) calculated by a radiative transfer model (Aoki et al., 1999, 2003) shown in Table 3.  
349 Values of  $SW_d$  and  $NIR_d$  that were outside the range were flagged as erroneous (–9999).

350 To recognize other instances when the radiation sensor was covered with snow or frost,  $SW_d$  and  
351  $NIR_d$  records corresponding to the following case that downward radiation is smaller than upward

352 radiation was flagged as erroneous (–9998), using  $SW_{\chi}$  as an example:

$$353 \quad SW_d < SW_u. \quad (2.3.1)$$

354 Figure 3c shows that the initial control eliminated a few erroneous  $SW_d$  data recorded in August 2015,  
355 whereas the secondary control masked many records, especially in February–May, that were affected  
356 by riming or frost.

#### 357 4.2.4. Shortwave and near-infrared albedo

358 We calculated albedos  $a_{sw}$  and  $a_{nir}$  from the  $SW_d$  and  $NIR_d$  datasets that were ~~passed~~ the  
359 secondary control. This calculation was done in four separate steps, shown by the color of dots in Fig.  
360 3d.

##### 361 (1) Flagging for low pyranometer sensitivity

362 At solar zenith angles near  $90.0^\circ$ ,  $SW_d$  and  $NIR_d$  may not be an accurate measurement because of  
363 the low sensitivity of the pyranometer. We therefore masked  $a_{sw}$  and  $a_{nir}$  values at  $solz > 85.0^\circ$  or when  
364 the  $SW_d$  ( $NIR_d$ ) value was below the median  $SW_d$  ( $NIR_d$ ) value for  $solz > 85.0^\circ$ . Records masked in this  
365 step are shown in Fig. 3d as light blue dots (d-i).

##### 366 (2) Range test for cold and warm periods

367 The range test used the upper and lower thresholds for  $a_{sw}$  and  $a_{nir}$  shown in Table 3, as determined  
368 by the radiative transfer calculation of Aoki et al. (2003, 2011) plus a small error margin. Those  
369 thresholds correspond to the assumed surface conditions during two parts of the year. For the cold  
370 period of October–April, we used the lower thresholds for dry snow at the SIGMA-A site and dry or  
371 wet snow at the SIGMA-B site conditions. For the warm period of May–September we used the  
372 thresholds for wet snow at the SIGMA-A site and wet snow or dark ice at the SIGMA-B site conditions.  
373 Records with albedo values beyond these theoretical thresholds were masked.

##### 374 (3) Anomaly test in low atmospheric transmittance condition

375 The range test was augmented by an anomaly test to identify underestimates of  $a_{sw}$  and  $a_{nir}$  when  
376  $SW_d$  ( $NIR_d$ ) was low and atmospheric transmittance ( $t_r$ ) was small, typically at large solar zenith angles.  
377 We masked  $a_{sw}$  ( $a_{nir}$ ) values that were unnaturally low owing to low  $t_r$  and  $SW_d$  ( $NIR_d$ ) in  $solz > 80.0^\circ$   
378 condition. Data records that were masked in either the range or anomaly tests are shown in Fig. 3d as  
379 red dots (d-ii).

##### 380 (4) Final steps

381 In cases where  $LW_d$  was flagged as “–9998” during the initial control (see Sect. 4.1.4),  $a_{sw}$  and  $a_{nir}$   
382 were flagged as “–9999” under the assumption that the radiation sensors were covered with snow or  
383 frost. The final step was a manual mask procedure. Data records that were masked in this phase are  
384 shown in Fig. 3d as orange dots (d-iii), and the final Level 1.3 dataset is displayed as blue dots (d-iv).

#### 385 4.2.5. Longwave radiation

386 The anomaly test for  $LW_d$  and  $LW_u$  was conducted only for the SIGMA-A dataset using a standard  
387 longwave radiant flux ( $LW_{std}$ ), a measure of the amount of longwave radiation from the near-surface  
388 atmosphere that was calculated from the air temperature measurement by Brock and Arnold (2000)

$$389 LW_{std} = \varepsilon^* \sigma (T_{2A} + 273.15)^4, \quad (xi)$$

$$390 \varepsilon^* = (1 + \kappa n) \varepsilon_0, \quad (xii)$$

$$391 \varepsilon_0 = 8.733 \times 10^{-3} \times (T_{2A} + 273.15)^{0.788}, \quad (xiii)$$

392 where  $\varepsilon^*$  is the atmospheric emissivity,  $\sigma$  ( $= 5.670 \times 10^{-8}$ ) is the Stefan–Boltzmann constant,  $\kappa$  ( $=$   
393  $0.26$ ) is a constant depending on cloud type (Braithwaite and Olsen, 1990),  $n$  is the cloud cover  
394 amount ( $n$ :  $[0, 1]$  and set at  $0.5$  because it could not be determined), and  $\varepsilon_0$  is the clear-sky emissivity.  
395 We assumed that  $LW_{std}$  was a close approximation of the true longwave radiant fluxes and used the  
396 absolute difference between  $LW_{std}$  and  $LW_d$  or  $LW_u$  (i.e.,  $\Delta LW_d$  or  $\Delta LW_u$ ) and its median and SD as the  
397 basis of the anomaly test as following Procedure 2.0.1.

398 Because parts of the  $LW_d$  dataset contained many erroneous records attributed to degradation of  
399 the data logger (see Fig. 3e), we reduced the SD criterion ( $\gamma = 1$ ) in 7 April to 7 June 2017 and after 1  
400 September 2017. Except for those two periods,  $\gamma$  was set to “2” for both  $\Delta LW_d$  and  $\Delta LW_u$ .  $LW_d$  and  
401  $LW_u$  records that were outliers under the criteria were flagged as erroneous (–9999). Figure 3e shows  
402 that the initial control (see Sect. 4.1.4) improved this anomaly test’s efficacy, and the secondary control  
403 yielded a clean  $LW_d$  time series.

#### 404 4.2.6. Surface height

405 The anomaly test for surface height masked data that displayed unrealistic fluctuations.  
406 Differences ( $\Delta sh$ ) were determined with respect to mean and SD values from the preceding 72 h values  
407 during period 1, before 1 September 2017 ( $sh_{mean1}$ ) and period 2, after 1 September 2017 ( $sh_{mean2}$ ). The  
408  $\Delta sh$  values were compared to the median plus SD of  $\Delta sh$  for that period. In the period 1, the SD  
409 criterion in Procedure 2.0.1 was strict ( $\gamma = 1$ ), and in the period 2, the criterion was relaxed ( $\gamma = 3$ ). In  
410 addition, because surface height increased steadily in period 2, we derived the regression equation for  
411 this increase and identified outliers with respect to the SD of the regression, i.e.  $\Delta sh_{reg}$  as follows:

$$412 \Delta sh_{reg} < SD_{reg-sh} \quad \text{for after 1 September 2017.} \quad (2.6.1)$$

413 Records of  $sh$  that varied beyond the anomaly ranges were flagged as erroneous (–9999).

414 A manual mask procedure was added as a final step. The result of QC procedure is shown in Fig.  
415 3f. The initial control, which corrected gaps resulting from the AWS maintenance (see Sect. 4.1.5),  
416 yielded the smoothed data record that enabled the application of the anomaly test. Sensor height dataset  
417 was made using initial sensor height (3 or 6 m) and the QC completed temporal surface height data.  
418 Therefore, QC for sensor height data has already been implemented through the QC for surface height

419 data.

#### 420 4.2.7. Snow temperature

421 In the first step, data records were masked when the snow temperature sensor was suspected to be  
422 located above the snow surface:

$$423 \quad st\_depth_n < -1.0 \rightarrow st_n \text{ flagged } -9999. \quad (2.7.1)$$

424 where  $st\_depth_n$  [cm] was calculated using surface height data and the initial setting depth of sensor  
425 “n” (see Sect. 3). The threshold of  $st\_depth_n$  included a margin of 1.0 cm to reflect the accuracy of the  
426 surface height sensor. The  $st_n$  was flagged as “-9997” if we could not judge whether the snow  
427 temperature sensor was located below the snow surface.

428 The anomaly test for  $st_n$  consisted of two procedures. The first procedure relied on a temperature  
429 gap ( $\Delta st_{d1}$ ) between  $st_4$  and data from each of the other five levels ( $st_{not4}$ ) (i.e.,  $\Delta st_{d1} = |st_4 - st_{not4}|$ ),  
430 because  $st_4$  had very few erroneous data. The SD criterion ( $\gamma$ ) for this anomaly test was changed for  
431 each parameter depending on the variability of the data. The second procedure used the difference  
432 ( $\Delta st_{d2}$ ) between  $st_n$  and its mean value  $st_{n\_mean}$  from the previous 72 h ( $\Delta st_{d2} = |st_n - st_{n\_mean}|$ ),  
433 calculated using the same method as  $sh_{mean}$  (see Sect. 4.2.6). The SD criteria ( $\gamma$ ) were all unity in this  
434 test. In both procedures, the median and SD terms were calculated from records for the full time period.  
435 Records detected as outliers were flagged as “-9999”. Figure 3g shows the results of all procedures,  
436 using  $st_3$  as an example.

#### 437 4.2.8. Atmospheric pressure

438 The time series of  $P_a$  included only a few erroneous records. We masked outliers on the basis of

$$439 \quad |P_a - P_{a\_mean}| > 20.0, \quad (2.8.1)$$

440 where  $P_{a\_mean}$  is the average for the past 3 h (excluding masked data records). We set the threshold at  
441 20.0, a higher value than the SD, because using the SD could have masked valid records. [This](#)  
442 [threshold value of 20 hPa is set on the assumption that a 20 hPa pressure jump is unlikely to occur in](#)  
443 [a few hours. This procedure success to mask properly only the erroneous data of both sites.](#)

### 444 5. Temporal variations of meteorological parameters

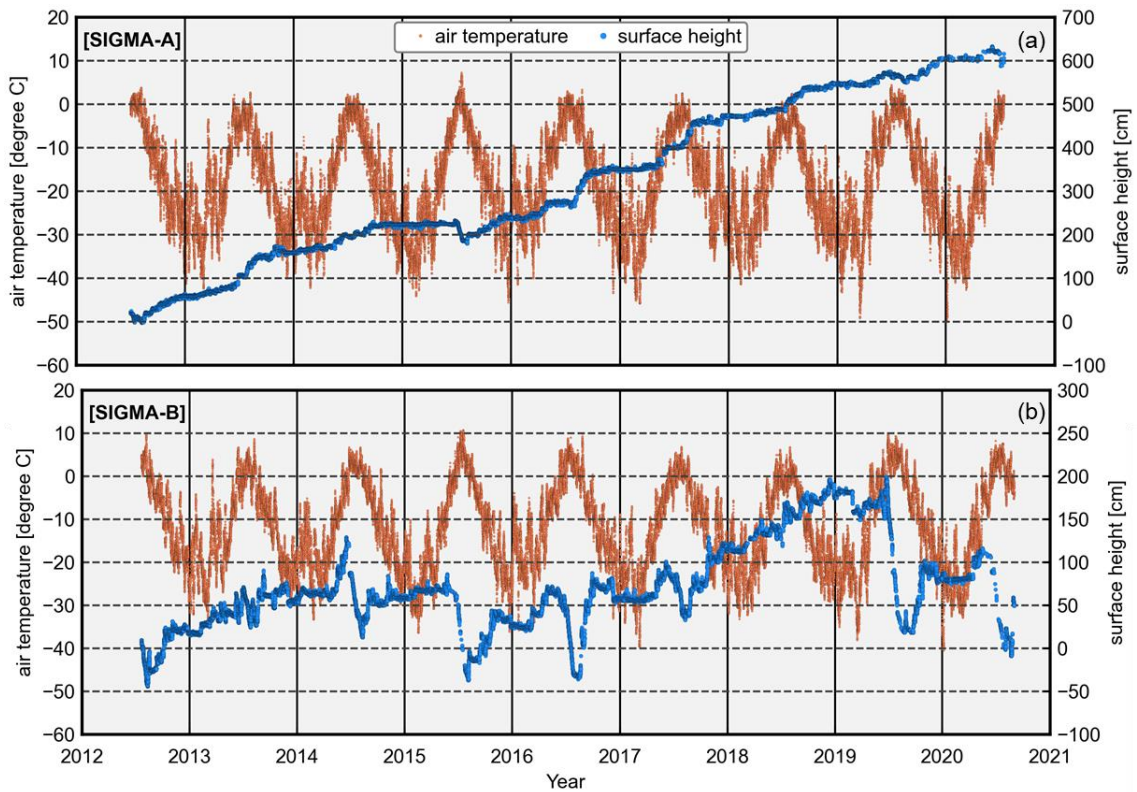
445 This section shows the results of simple analyses of the Level 1.3 dataset.

#### 446 5.1. Air temperature and surface height

447 Figure 4 shows the air temperature fluctuations and surface height ( $sh$ ) variations at both sites.  
448 Mean air temperatures (2013–2019) were  $-18.1$  °C at the SIGMA-A site and  $-12.3$  °C at the SIGMA-

449 B site. The annual maxima of monthly data were recorded every July at both sites, except for August  
 450 2019 at the SIGMA-B site. At the SIGMA-A site, The that annual maximum in 2015 was slightly  
 451 positive (+0.1 °C in July) but others were negative. at the SIGMA-A site, and At the SIGMA-B site,  
 452 it those were above freezing in all years at the SIGMA-B site. In contrast, tThe annual minima  
 453 occurred in different months between December and March. ~~The maximum was slightly positive at~~  
 454 ~~the SIGMA-A site, and it was above freezing in all years at the SIGMA-B site.~~ Unusually high hourly  
 455 temperatures were recorded in mid-July 2015 (7.2 °C at SIGMA-A and 10.7 °C at SIGMA-B). Air  
 456 temperatures exceeding 5.0 °C at SIGMA-A and 10.0 °C at SIGMA-B were common during that  
 457 period.

458 Surface height steadily increased at the SIGMA-A site during the 8-year study period (Fig. 4), in  
 459 which *sh* rose approximately 1 m in the mass-balance years (September to August) of 2013/14,  
 460 2016/17, and 2017/18, and decreased slightly in the summers of 2011/12, 2014/15, and 2019/20.  
 461 Accumulations were notable in autumn and relatively small in winter. At the SIGMA-B site, in contrast,  
 462 increases and decreases in *sh* were observed during each mass-balance year. Decreases in *sh* during  
 463 summers were rare during the summers of 2012/13 and 2017/18 but common during the 2013/14,  
 464 2014/15, 2015/16, 2018/19, and 2019/20 summers, when decreases were greater than 1 m.  
 465



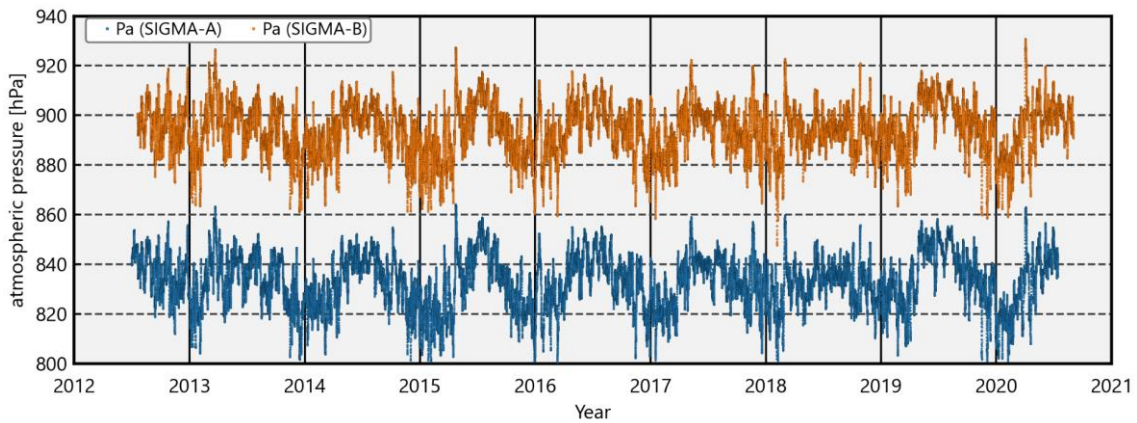
466  
 467 Figure 4. Time series of hourly air temperature and surface height at the (a) SIGMA-A (showing  $T_2$   
 468 data) and (b) SIGMA-B sites.

469

## 470 5.2. Atmospheric pressure and seasonal variation of temperature lapse rate

471 The time series of atmospheric pressure ( $P_a$ ) at the SIGMA-A and SIGMA-B sites show a clear  
472 seasonal variation, high in summer and low in winter (Fig. 6). The two data records had similar  
473 variation patterns that were strongly correlated ( $r = 0.98$ ). The mean values for the whole observation  
474 period were 833.1 hPa at site SIGMA-A and 894.2 hPa at site SIGMA-B (Table 4). The difference in  
475 monthly mean  $P_a$  between the sites was smaller in summer and larger in winter (Fig. 7a), and the  
476 amplitude of the annual cycle was greater at the SIGMA-A site.

477

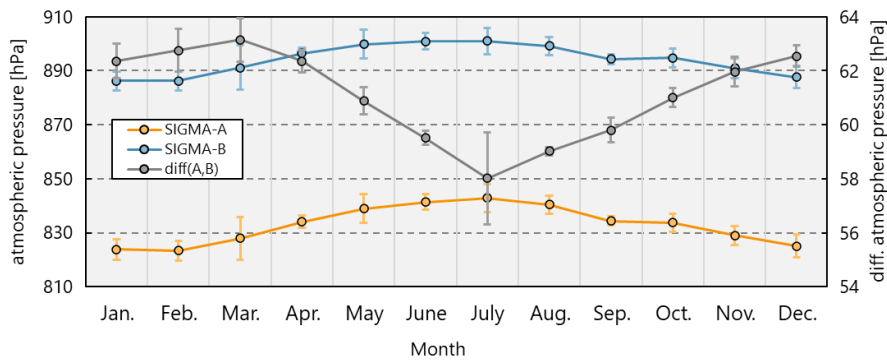


478

479 Figure 6. Time series of hourly atmospheric pressure ( $P_a$ ) at the SIGMA-A and SIGMA-B sites.

480

481



482

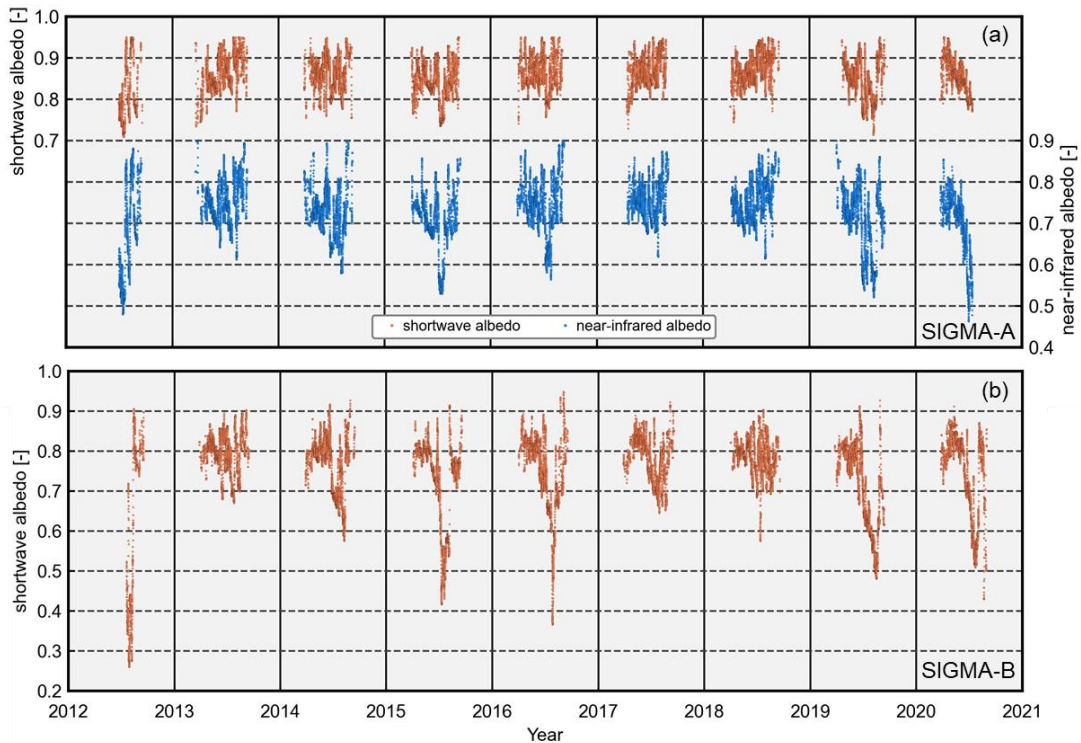
483 Figure 7. Time series of ensemble averages of monthly mean atmospheric pressures during all years  
484 at both sites and their difference. Error bars indicate  $\pm 1$  SD.

485

## 486 5.3. Albedo

487 Whereas shortwave albedo ( $a_{sw}$ ) was rarely lower than 0.7 at site SIGMA-A, near-infrared albedo

488 ( $a_{\text{nir}}$ ) was below 0.6 in 2012, 2015, 2016, 2019, and 2020 (Fig. 8). Because  $a_{\text{nir}}$  depends on the snow  
 489 grain size (Wiscombe and Warren, 1980), this finding implies that snow metamorphism progressed at  
 490 the SIGMA-A site in those years (Hirose et al., 2021). A strong decrease in  $a_{\text{sw}}$  was observed at the  
 491 SIGMA-B site during those same summers, which corresponded to notable decreases in surface height  
 492 (Fig. 4b) and high PDDs (Fig. 5). The decreases in albedo may have accelerated snowmelt and caused  
 493 the decreases in surface height at SIGMA-B during the warm summers of those years (see Sect. 5.1).  
 494 It appears that the difference in albedo reduction between the SIGMA-A and SIGMA-B sites in  
 495 summer originated from the difference in air temperature between the sites.  
 496  
 497



498  
 499 Figure 8. Time series of hourly shortwave and near-infrared albedos at the (a) SIGMA-A and (b)  
 500 SIGMA-B sites.  
 501

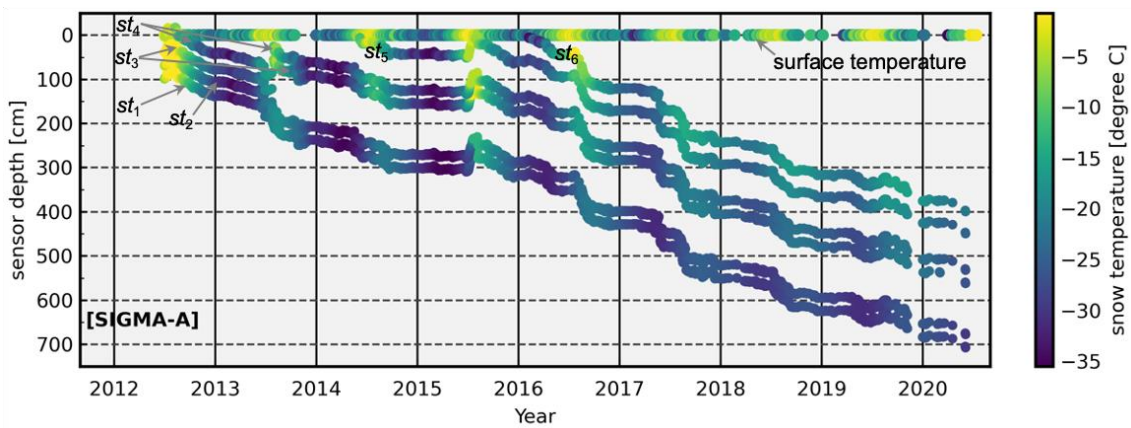
502 **5.4. Snow temperature**

503 Figure 9 shows the time series of snow temperatures ( $st_1$ – $st_6$ ) and snow sensor depths ( $st\_depth_1$ –  
 504  $st\_depth_6$ ). The sensor depths were calculated from each sensor’s initial depths (see Sect. 3.1) and the surface  
 505 height variations at the SIGMA-A site. Seasonal and short-term snow temperature fluctuations were  
 506 observed, which became smaller after the 2016/17 winter season, when snow accumulation was very  
 507 large (Fig. 4). We assumed that the sensors were buried more deeply at that time, resulting in smaller

508 fluctuations in snow temperature. The annual mean snow temperatures after 2016, a year in which  
 509 snow temperatures were relatively stable and less variable, were between  $-18.9 \pm 0.5$  °C ( $st_4$ ) and  
 510  $-19.5 \pm 1.7$  °C ( $st_5$ ).

511 Sensors recorded relatively high snow temperatures when they were positioned at shallow depths  
 512 below the snow surface. However, in the summer of 2015, sensors  $st_3$  and  $st_4$  registered 0 °C even  
 513 though they were more than 1 m below the snow surface. Air temperatures above freezing, and a large  
 514 decrease in surface height were observed in this period (Figs. 4 and 5); thus, it is plausible that  
 515 snowmelt occurred from the surface to depths near 120 cm, where  $st_3$  was located at that time.

516



517

518 Figure 9. Time series of hourly snow temperatures ( $st_1$ – $st_6$ ), sensor depth, and surface temperature  
 519 (calculated from upward longwave radiation) at the SIGMA-A site.

520

## 521 5.5. Longwave radiation

522

The ~~occurrence~~-frequency distribution of longwave radiation, taken to represent the atmospheric  
 523 condition, is often used as an indicator of climatological cloudiness (Stramler et al., 2011). Figure 10  
 524 shows the histograms of occurrence frequency of downward ( $LW_d$ ) and net longwave radiation ( $LW_{net}$   
 525 =  $LW_d - LW_u$ ) during July of all years at the SIGMA-A and SIGMA-B sites. The corresponding  
 526 histograms for the four seasons (autumn: SON, winter: DJF, spring: MAM, summer: JJA) are shown  
 527 in Figs. S1 and S2. The July  $LW_d$  data from both sites had bimodal distributions, with a lower mode  
 528 of 220–240  $W m^{-2}$  at SIGMA-A and 240–260  $W m^{-2}$  at SIGMA-B, and a higher mode of 290–310  $W$   
 529  $m^{-2}$  at SIGMA-A and 310–330  $W m^{-2}$  at SIGMA-B. The histograms of July and seasonal  $LW_{net}$  had  
 530 similar but clearer bimodal distributions, with modes at approximately 0  $W m^{-2}$  and  $-70 W m^{-2}$  (Figs.  
 531 10c-d and S2).

532

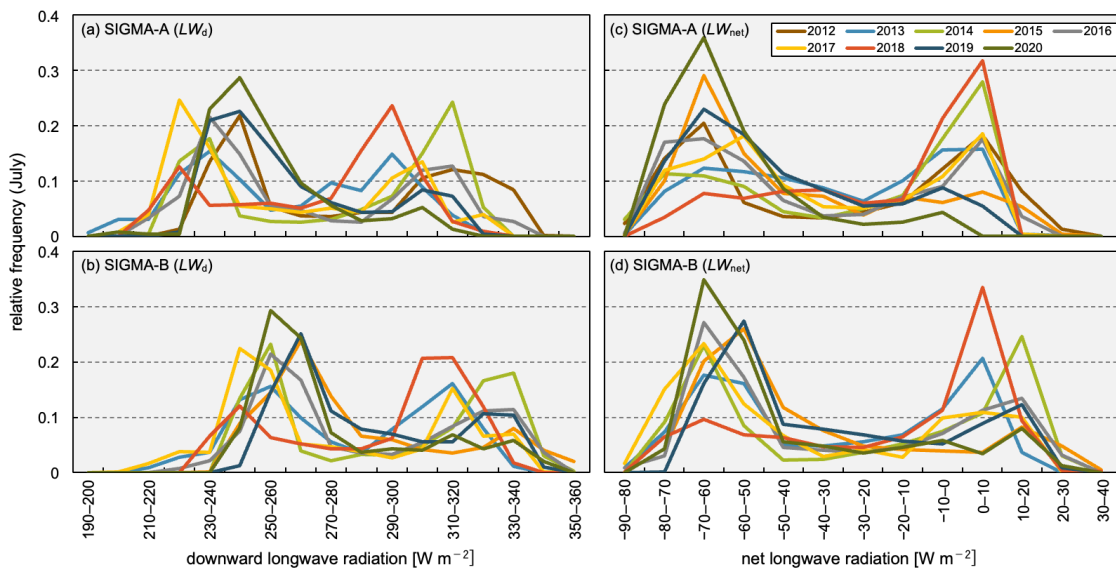
$LW_{net}$  can be regarded as an indicator of cloudiness, ~~which can significantly change the downward~~  
 533 ~~longwave radiation and thus the surface temperature of the snow or ice, because blackbody radiation~~  
 534 ~~from the cloud cover increase~~ Both downward and net longwave radiation ~~increase under overcast~~



535 ~~conditions because of blackbody radiation from the cloud cover that is absent in clear-sky conditions.~~

536 Stramler et al. (2011) and Morrison et al. (2012) have argued that surface net longwave radiative flux  
537 has two modes in occurrence frequency (at  $-40 \text{ W m}^{-2}$  and  $0 \text{ W m}^{-2}$ ), which correspond to clear-sky  
538 and overcast (low-level mixed-phase clouds) conditions. In overcast conditions, because the cloud  
539 base and the surface are in thermal equilibrium, the vertical thermal gradient is small and the longwave  
540 radiation budget is balanced ( $LW_{\text{net}} = 0 \text{ W m}^{-2}$ ) at the surface. The two modes of  $LW_{\text{net}}$  ( $0 \text{ W m}^{-2}$  and  
541  $-70 \text{ W m}^{-2}$ ) at the two AWS sites appear to correspond to the modes proposed by these earlier studies.

542 The occurrence frequency of  $LW_{\text{net}}$  in JJA appears to be more variable than those for the other  
543 seasons at both sites (Fig. S2). In these months, the air temperature rises and sea ice extent decreases,  
544 increasing the water vapor supply and advection from the surrounding sea to coastal Greenland (Kim  
545 and Kim, 2017; Liang et al., 2022). In such atmospheric conditions, the cloud formation process is  
546 susceptible to synoptic-scale disturbances. The histogram of  $LW_{\text{net}}$  for July (Fig. 10) indicates a higher  
547 frequency of clear-sky ( $LW_{\text{net}} \cong -70 \text{ W m}^{-2}$ ) in 2015, 2019, and 2020 and overcast conditions ( $LW_{\text{net}}$   
548  $\cong 0 \text{ W m}^{-2}$ ) in 2014 and 2018. In SON and MAM, weather condition was less variable, and overcast  
549 and clear-sky conditions dominated, respectively. In contrast, annual occurrence frequencies for SON  
550 and MAM were less variable than those for JJA. Overcast and clear sky conditions dominated in SON  
551 and MAM, respectively. Our analysis shows that cloudiness in JJA was more variable than in other  
552 seasons, a result that is also borne out by satellite observations (Ryan et al., 2022).



554 Figure 10. Histograms of the occurrence frequency of hourly downward longwave radiation ( $LW_d$ ) and  
555 net longwave radiation ( $LW_{\text{net}}$ ) observed at the SIGMA-A and SIGMA-B sites in July of all years in  
556 the study period. Each relative frequency represents the fraction of the total contained in each  $10 \text{ W}$   
557  $\text{m}^{-2}$  bin.  
558

559 **6. Data availability**

560 The Level 1.1, 1.2, and 1.3 datasets from this study are archived and available from the Arctic Data  
561 archive System (ADS) in the National Institute of Polar Research (Table 6), where they are stored in  
562 text (CSV) file format. Detailed information on the data content is presented in the file  
563 “data\_format\_site-name\_data-level.csv” associated with each of these dataset files.

564

565 Table 6. Information for the archived datasets from the SIGMA-A and SIGMA-B sites.

<i>SIGMA-A</i>	
Level 1.1	
data name:	Quality-controlled datasets of Automatic Weather Station (AWS) at SIGMA-A site from 2012 to 2020: Level: 1.1
file name:	SIGMA_AWS_SiteA_2012-2020_Lv1_1.csv
citation:	<a href="http://doi.org/10.17592/001.2022041301">http://doi.org/10.17592/001.2022041301</a>
reference:	Nishimura et al. (2023a)
Level 1.2	
data name:	Quality-controlled datasets of Automatic Weather Station (AWS) at SIGMA-A site from 2012 to 2020: Level: 1.2
file name:	SIGMA_AWS_SiteA_2012-2020_Lv1_2.csv
citation:	<a href="http://doi.org/10.17592/001.2022041302">http://doi.org/10.17592/001.2022041302</a>
reference:	Nishimura et al. (2023b)
Level 1.3	
data name:	Quality-controlled datasets of Automatic Weather Station (AWS) at SIGMA-A site from 2012 to 2020: Level: 1.3
file name:	SIGMA_AWS_SiteA_2012-2020_Lv1_3.csv
citation:	<a href="http://doi.org/10.17592/001.2022041303">http://doi.org/10.17592/001.2022041303</a>
reference:	Nishimura et al. (2023c)
<i>SIGMA-B</i>	
Level 1.1	
data name:	Quality-controlled datasets of Automatic Weather Station (AWS) at SIGMA-B site from 2012 to 2020: Level 1.1
file name:	SIGMA_AWS_SiteB_2012-2020_Lv1_1.csv
citation:	<a href="http://doi.org/10.17592/001.2022041304">http://doi.org/10.17592/001.2022041304</a>
reference:	Nishimura et al. (2023d)
Level 1.2	
data name:	Quality-controlled datasets of Automatic Weather Station (AWS) at SIGMA-B site from 2012 to 2020: Level 1.2
file name:	SIGMA_AWS_SiteB_2012-2020_Lv1_2.csv
citation:	<a href="http://doi.org/10.17592/001.2022041305">http://doi.org/10.17592/001.2022041305</a>
reference:	Nishimura et al. (2023e)
Level 1.3	
data name:	Quality-controlled datasets of Automatic Weather Station (AWS) at SIGMA-B site from 2012 to 2020: Level 1.3
file name:	SIGMA_AWS_SiteB_2012-2020_Lv1_3.csv
citation:	<a href="http://doi.org/10.17592/001.2022041306">http://doi.org/10.17592/001.2022041306</a>
reference:	Nishimura et al. (2023f)

566

567 **7. Summary and conclusion**

568 This paper describes the in situ meteorological datasets from the SIGMA-A and SIGMA-B AWS  
569 sites in northwest Greenland and details the QC methods used in preparing the datasets. At this time  
570 when drastic environmental change is proceeding in the Arctic region, sound meteorological data and

571 QC methods are of ever-growing importance.

572 The QC method offered here consists of two basic steps. The first step, the initial control, masks  
573 observations that are affected by mechanical malfunctions or local phenomena and is a pre-treatment  
574 for the second QC step. This step uses simple statistics to set the range of permissible variation in  
575 northwest Greenland for each observational parameter and flags erroneous records on the basis of that  
576 variation range. The second QC step, the secondary control, masks erroneous observations based on  
577 more stringent variation ranges as determined by the median and SD values of the full observation  
578 record. The QC procedures offered here may be valuable for scientists developing their own QC efforts.

579 We presented examples of time series of air temperature, surface height, atmospheric pressure,  
580 snow temperature, surface albedos, and longwave radiation based on the resulting hourly  
581 meteorological dataset for 2012–2020 in northwest Greenland. We also extracted information on  
582 climatological cloudiness based on  $LW_{\text{net}}$  data derived from these in situ ground observations. Our  
583 primary findings are summarized in the following four points: (1) ~~in the 2015 summer,~~ high air  
584 temperature ~~in the 2015 summer and, in addition, 2016, 2019, 2020 summers~~ low surface albedos ~~in~~  
585 ~~2016, 2019, and 2020 summers~~ were recorded at both SIGMA-A and SIGMA-B sites. (2)  
586 ~~Apparent~~~~Dramatic~~ decreases in surface height occurred in 2015 at both AWS sites and in 2016, 2019,  
587 and 2020 at the SIGMA-B site. (3) ~~Observed atmospheric~~~~Weather~~ conditions in JJA were relatively  
588 variable in northwest Greenland compared to the other seasons. (4) ~~Frequent~~ ~~C~~clear-sky conditions  
589 typified the summers of 2015, 2019, and 2020.

590 The datasets described here are archived in the open access Arctic Data archive System for all  
591 scientific communities. We anticipate that they will not only aid in understanding and monitoring the  
592 current climate in northwest Greenland but also contribute more broadly to the advancement of polar  
593 climate studies.

594

### 595 **Author contribution**

596 All authors, excluding M. Nishimura, established the AWS systems and supported their  
597 maintenance. In addition, M. Nishimura developed and carried out the QC procedures and analyzed  
598 the observation data, TA designed and led the study project and provided technical support for the QC  
599 procedures, M. Niwano conducted pre-treatments for the meteorological data record and constructed  
600 a fundamental algorithm of the QC procedures, TY supported the field observations, especially  
601 logistical support, and KF provided advice on interpreting the observational data. All authors  
602 participated in the interpretation of results and gave final approval for publication.

### 603 **Competing interests**

604 The authors declare that they have no conflict of interest.

## 605 Acknowledgments

606 We recognize all members of the SIGMA project, the GRENE-Arctic Project in Greenland, and  
607 the Arctic Challenge for Sustainability II (ArCS II) project. We also thank all of those who supported  
608 the field observations. In particular, we thank Y. Iizuka (Hokkaido University), Y. Kurosaki (Hokkaido  
609 University), and A. Tsushima (Chiba University) for taking part in the field activities at the SIGMA-  
610 A site and establishing the AWS and Y. Komuro (National Institute of Polar Research) for technical  
611 advice. This study was conducted as a part of the “Snow Impurity and Glacial Microbe effects on  
612 abrupt warming in the Arctic (SIGMA)” Project supported by the Japan Society for the Promotion of  
613 Science Grant-in-Aid for Scientific Research numbers JP23221004 and JP16H01772, the Global  
614 Change Observation Mission-Climate (GCOM-C) research project of the Japan Aerospace  
615 Exploration Agency, and ArCS II Program Grant Number JPMXD1420318865. For the use of  
616 NunaGIS (<http://en.nunagis.gl/>) operated by Asiaq, Greenland Survey, in preparing Fig. 1, we  
617 acknowledge the National Snow and Ice Data Center’s QGreenland package (Moon et al., 2021). The  
618 DEM data from Arctic DEMs were provided by the Polar Geospatial Center under NSF-OPP awards  
619 1043681, 1559691, and 1542736. Finally, we are grateful to the two anonymous reviewers and to B.  
620 Vandecrux and G. Wolfgang as reviewers, as well as to Topical Editor G. Tobias for their very helpful  
621 comments on the manuscript. Their comments have greatly refined and enhanced the value of this  
622 paper.

## 623 References

- 624 Aoki, T., Aoki, T., Fukabori, M., and Uchiyama, A.: Numerical simulation of the atmospheric effects  
625 on snow albedo with a multiple scattering radiative transfer model for the atmosphere-snow system,  
626 J. Meteorol. Soc. Japan, 77, 595-614, [https://doi.org/10.2151/jmsj1965.77.2\\_595](https://doi.org/10.2151/jmsj1965.77.2_595), 1999.
- 627 Aoki, T., Kuchiki, K., Niwano, M., Kodama, Y., Hosaka, M., and Tanaka, T.: Physically based snow  
628 albedo model for calculating broadband albedos and the solar heating profile in snowpack for  
629 general circulation models. J. Geophys. Res.: Atmos., 116 (D11114), 1–22.  
630 <https://doi.org/10.1029/2010JD015507>, 2011.
- 631 Aoki, T., Hachikubo, A., and Hori, M.: Effect of snow physical parameters on shortwave broadband  
632 albedos, J. Geophys. Res., 108, D19, 1–12. <https://doi.org/10.1029/2003jd003506>, 2003.
- 633 Aoki, T., Matoba, S., Uetake, J., Takeuchi, N., and Motoyama, H.: Field activities of the “Snow  
634 Impurity and Glacial Microbe effects on abrupt warming in the Arctic” (SIGMA) Project in  
635 Greenland in 2011-2013. Bull. Glaciol. Res., 32, 3–20. <https://doi.org/10.5331/bgr.32.3>, 2014.
- 636 Armstrong, R. L. and Brun, E. (Eds.): Physical processes within the snow cover and their  
637 parameterization, in Snow and Climate: Physical Processes, Surface Energy Exchange and  
638 Modeling, Cambridge University Press, Cambridge N.Y., p. 58, 2008.

639 Behrens, K.: Radiation sensors, in: Springer handbook of atmospheric measurements, edited by: Foken,  
640 T., Springer International Publishing, pp. 297–357, [https://doi.org/10.1007/978-3-030-52171-](https://doi.org/10.1007/978-3-030-52171-4_11)  
641 [4\\_11](https://doi.org/10.1007/978-3-030-52171-4_11), 2021.

642 Braithwaite, R. J. and Olesen, O. B.: A simple energy-balance model to calculate ice ablation at the  
643 margin of the Greenland ice sheet. *J. Glaciol.*, 36, 222–228.  
644 <https://doi.org/10.1017/S0022143000009473>, 1990.

645 Brock, B. W. and Arnold, N. S.: A spreadsheet-based (Microsoft Excel) point surface energy balance  
646 model for glacier and snow melt studies. *Earth Surf. Proc. Land.*, 25, 649–658.  
647 [https://doi.org/10.1002/1096-9837\(200006\)25:6<649::AID-ESP97>3.0.CO;2-U](https://doi.org/10.1002/1096-9837(200006)25:6<649::AID-ESP97>3.0.CO;2-U), 2000.

648 Estévez, J., Gavilán, P., and Giráldez, J. V.: Guidelines on validation procedures for meteorological  
649 data from automatic weather stations, *J. Hydrol.*, 402, 144–154.  
650 <https://doi.org/10.1016/j.jhydrol.2011.02.031>, 2011.

651 Fausto, R. S., van As, D., Mankoff, K. D., Vandecrux, B., Citterio, M., Ahlstrøm, A. P., Andersen, S.  
652 B., Colgan, W., Karlsson, N. B., Kjeldsen, K. K., Korsgaard, N. J., Larsen, S. H., Nielsen, S.,  
653 Pedersen, A., Shields, C. L., Solgaard, A. M., and Box, J. E.: Programme for Monitoring of the  
654 Greenland Ice Sheet (PROMICE) automatic weather station data. *Earth Syst. Sci. Data*, 13, 3819–  
655 3845. <https://doi.org/10.5194/essd-13-3819-2021>, 2021.

656 Fiebrich, C. A., Morgan, Y. R., McCombs, A. G., Hall, P. K., and McPherson, R. A.: Quality assurance  
657 procedures for mesoscale meteorological data. *J. Atmos. Ocean. Tech.*, 27, 1565–1582.  
658 <https://doi.org/10.1175/2010JTECHA1433.1>, 2010.

659 Fröhlich, C.: Total solar irradiance observations. *Surv. Geophys*, 33, 453–473.  
660 <https://doi.org/10.1007/s10712-011-9168-5>, 2012.

661 Fujita, K., Matoba, S., Iizuka, Y., Takeuchi, N., Tsushima, A., Kurosaki, Y., and Aoki, T.: Physically  
662 based summer temperature reconstruction from melt layers in ice cores. *Earth Space Sci.*,  
663 8(e2020EA001590), 1–17. <https://doi.org/10.1029/2020EA001590>, 2021.

664 Hirose, S., Aoki, T., Niwano, M., Matoba, S., Tanikawa T., Yamaguchi, S., , and Yamasaki, T.:  
665 Surface energy balance observed at the SIGMA-A site on the northwest Greenland ice sheet (in  
666 Japanese with English abstract). *Seppyo*, 83, 143–154, [https://doi.org/10.5331/seppyo.83.2\\_143](https://doi.org/10.5331/seppyo.83.2_143),  
667 2021.

668 Hock, R. and Holmgren, B.: A distributed surface energy-balance model for complex topography and  
669 its application to Storglaciären, Sweden, *J. Glaciol.*, 51, 25–36.  
670 <https://doi.org/10.3189/172756505781829566>, 2005.

671 Jonsell, U., Hock, R., and Holmgren, B.: Spatial and temporal variations in albedo on Storglaciären,  
672 Sweden, *J. Glaciol.*, 49, 59–68. <https://doi.org/10.3189/172756503781830980>, 2003.

673 Kim, H. M. and Kim, B. M.: Relative contributions of atmospheric energy transport and sea ice loss  
674 to the recent warm arctic winter. *J. Clim.*, 30, 7441–7450. <https://doi.org/10.1175/JCLI-D-17->

675 0157.1, 2017.

676 Kurosaki, Y., Matoba, S., Iizuka, Y., Niwano, M., Tanikawa, T., Ando, T., Hori, A., Miyamoto, A.,  
677 Fujita, S., and Aoki, T.: Reconstruction of sea ice concentration in northern Baffin Bay using  
678 deuterium excess in a coastal ice core from the north-western Greenland Ice Sheet. *J. Geophys.*  
679 *Res. Atmos.*, 125. <https://doi.org/10.1029/2019JD031668>, 2020.

680 Liang, Y., Bi, H., Huang, H., Lei, R., Liang, X., Cheng, B., and Wang, Y.: Contribution of warm and  
681 moist atmospheric flow to a record minimum July sea ice extent of the Arctic in 2020. *The*  
682 *Cryosphere*, 16, 1107–1123. <https://doi.org/10.5194/tc-16-1107-2022>, 2022.

683 Makkonen, L. and Laakso, T.: Humidity measurements in cold and humid environments. *Boundary-*  
684 *Layer Meteorol.*, 116, 131–147. <https://doi.org/10.1007/s10546-004-7955-y>, 2005.

685 Matoba, S., Niwano, M., Tanikawa, T., Iizuka, Y., Yamasaki, T., Kurosaki, Y., Aoki, T., Hashimoto,  
686 A., Hosaka, M., and Sugiyama, S.: Field activities at the SIGMA-A site, north-western Greenland  
687 Ice Sheet, 2017. *Bull. Glaciol. Res.*, 36, 15–22. <https://doi.org/10.5331/BGR.18R01>, 2018.

688 Matoba, S., Yamaguchi, S., Tsushima, A., Aoki, T., and Sugiyama, S.: Surface mass balance variations  
689 in a maritime area of the north-western Greenland Ice Sheet (in Japanese with English abstract).  
690 *Low Temperature Science*, 75, 37–44, doi: 10.14943/lowtemsci.75.37, 2017.

691 Moon, T., Fisher, M., Harden, L., and Stafford, T.: QGreenland (v1.0.1) [software]. Available from  
692 <https://qgreenland.org>. <https://doi.org/10.5281/zenodo.4558266>, 2021.

693 Moradi, I.: Quality control of global solar radiation using sunshine duration hours, *Energy*, 34, 1–6.  
694 <https://doi.org/10.1016/j.energy.2008.09.006>, 2009.

695 Morino, S., Kurita, N., Hirasawa, N., Motoyama, H., Sugiura, K., Lazzara, M., Mikolajczyk, D.,  
696 Welhouse, L., Keller, L., and Weidner, G.: Comparison of Ventilated and Unventilated Air  
697 Temperature Measurements in Inland Dronning Maud Land on the East Antarctic Plateau. *J.*  
698 *Atmos. and Ocean. Technol.*, 38, 2061–2070. <https://doi.org/10.1175/JTECH-D-21-0107.1>, 2021.

699 Morrison, H., De Boer, G., Feingold, G., Harrington, J., Shupe, M. D., and Sulia, K.: Resilience of  
700 persistent Arctic mixed-phase clouds. *Nat. Geosci.*, 5, 11–17. <https://doi.org/10.1038/ngeo1332>,  
701 2012.

702 Mougnot, J., Rignot, E., Bjørk, A. A., van den Broeke, M., Millan, R., Morlighem, M., Noël, B.,  
703 Scheuchl, B., and Wood, M.: Forty-six years of Greenland Ice Sheet mass balance from 1972 to  
704 2018, *P. Natl. Acad. Sci. USA*, 116, 9239–9244. <https://doi.org/10.1073/pnas.1904242116>, 2019.

705 Nishimura, M., T. Aoki, M. Niwano, S. Matoba, T. Tanikawa, S. Yamaguchi, T. Yamasaki, A.  
706 Tsushima, K. Fujita, Y. Iizuka, Y. Kurosaki: Quality-controlled datasets of Automatic Weather  
707 Station (AWS) at SIGMA-A site from 2012 to 2020: Level 1.1, 1.00, Arctic Data archive System  
708 (ADS), Japan [dataset], <http://doi.org/10.17592/001.2022041301>, 2023a.

709 Nishimura, M., T. Aoki, M. Niwano, S. Matoba, T. Tanikawa, S. Yamaguchi, T. Yamasaki, A.  
710 Tsushima, K. Fujita, Y. Iizuka, Y. Kurosaki: Quality-controlled datasets of Automatic Weather

711 Station (AWS) at SIGMA-A site from 2012 to 2020: Level 1.2, 1.20, Arctic Data archive System  
712 (ADS), Japan [dataset], <http://doi.org/10.17592/001.2022041302>, 2023b.

713 Nishimura, M., T. Aoki, M. Niwano, S. Matoba, T. Tanikawa, S. Yamaguchi, T. Yamasaki, A.  
714 Tsushima, K. Fujita, Y. Iizuka, Y. Kurosaki: Quality-controlled datasets of Automatic Weather  
715 Station (AWS) at SIGMA-A site from 2012 to 2020: Level 1.3, 1.20, Arctic Data archive System  
716 (ADS), Japan [dataset], <http://doi.org/10.17592/001.2022041303>, 2023c

717 Nishimura, M., T. Aoki, M. Niwano, S. Matoba, T. Tanikawa, S. Yamaguchi, T. Yamasaki, K. Fujita:  
718 Quality-controlled datasets of Automatic Weather Station (AWS) at SIGMA-B site from 2012 to  
719 2020: Level 1.1, 1.00, Arctic Data archive System (ADS), Japan [dataset],  
720 <http://doi.org/10.17592/001.2022041304>, 2023d.

721 Nishimura, M., T. Aoki, M. Niwano, S. Matoba, T. Tanikawa, S. Yamaguchi, T. Yamasaki, K. Fujita:  
722 Quality-controlled datasets of Automatic Weather Station (AWS) at SIGMA-B site from 2012 to  
723 2020: Level 1.2, 1.10, Arctic Data archive System (ADS), Japan [dataset],  
724 <http://doi.org/10.17592/001.2022041305>, 2023e.

725 Nishimura, M., T. Aoki, M. Niwano, S. Matoba, T. Tanikawa, S. Yamaguchi, T. Yamasaki, K. Fujita:  
726 Quality-controlled datasets of Automatic Weather Station (AWS) at SIGMA-B site from 2012 to  
727 2020: Level 1.3, 1.20, Arctic Data archive System (ADS), Japan [dataset],  
728 <http://doi.org/10.17592/001.2022041306>, 2023f.

729 Niwano, M., Aoki, T., Matoba, S., Yamaguchi, S., Tanikawa, T., Kuchiki, K., and Motoyama, H.:  
730 Numerical simulation of extreme snowmelt observed at the SIGMA-A site, northwest Greenland,  
731 during summer 2012. *The Cryosphere*, 9, 971–988. <https://doi.org/10.5194/tc-9-971-2015>, 2015.

732 Niwano, M., Aoki, T., Hashimoto, A., Matoba, S., Yamaguchi, S., Tanikawa, T., Fujita, K., Tsushima,  
733 A., Iizuka, Y., Shimada, R., and Hori, M.: NHM-SMAP: Spatially and temporally high-resolution  
734 nonhydrostatic atmospheric model coupled with detailed snow process model for Greenland Ice  
735 Sheet. *The Cryosphere*, 12, 635–655. <https://doi.org/10.5194/tc-12-635-2018>, 2018.

736 Niwano, M., Box, J. E., Wehrlé, A., Vandecrux, B., Colgan, W. T., and Cappelen, J.: Rainfall on the  
737 Greenland Ice Sheet: Present-day climatology from a high-resolution non-hydrostatic polar  
738 regional climate model. *Geophys. Res. Lett.*, 48(e2021GL092942), 1–11.  
739 <https://doi.org/10.1029/2021GL092942>, 2021.

740 Noël, B., van de Berg, W. J., Lhermitte, S., and van den Broeke, M. R.: Rapid ablation zone expansion  
741 amplifies north Greenland mass loss, *Sci. Adv.*, 5, 2–11. <https://doi.org/10.1126/sciadv.aaw0123>,  
742 2019.

743 Onuma, Y., Takeuchi, N., Tanaka, S., Nagatsuka, N., Niwano, M., and Aoki, T.: Observations and  
744 modelling of algal growth on a snowpack in north-western Greenland. *The Cryosphere*, 12, 2147–  
745 2158. <https://doi.org/10.5194/tc-12-2147-2018>, 2018.

746 Porter, C., Morin, P., Howat, I., Noh, M. J., Bates, B., Peterman, K., Keesey, S., Schlenk, M., Gardiner,  
747 J., Tomko, K., Willis, M., Kelleher, C., Cloutier, M., Husby, E., Foga, S., Nakamura, H., Platson,  
748 M., Wethington, M. Jr., Williamson, C., Bauer, G., Enos, J., Arnold, G., Kramer, W., Becker, P.,  
749 Doshi, A., D'Souza, C., Cummens, P., Laurier, F., Bojesen, M.: "ArcticDEM",  
750 <https://doi.org/10.7910/DVN/OHHUKH>, Harvard Dataverse, V1, [Accessed in January 18, 2022],  
751 2018.

752 Rottman, G.: Measurement of total and spectral solar irradiance. *Space Sci. Rev.*, 125, 39–51.  
753 <https://doi.org/10.1007/s11214-006-9045-6>, 2006.

754 Ryan, J. C., Smith, L. C., Cooley, S. W., Pearson, B., Wever, N., Keenan, E., and Lenaerts, J. T. M.:  
755 Decreasing surface albedo signifies a growing importance of clouds for Greenland Ice Sheet  
756 meltwater production. *Nat. Comm.*, 13(4205), 1–8. <https://doi.org/10.1038/s41467-022-31434-w>,  
757 2022.

758 Steffen, C. and Box, J. E.: Surface climatology of the Greenland ice sheet: Greenland Climate Network  
759 1995-1999, *J. Geophys. Res.*, 106, D24, 33951–33964, 2001.

760 Stramler, K., Del Genio, A. D., and Rossow, W. B.: Synoptically driven Arctic winter states. *J. Clim.*,  
761 24, 1747–1762. <https://doi.org/10.1175/2010JCLI3817.1>, 2011.

762 Sugiyama, S., Sakakibara, D., Matsuno, S., Yamaguchi, S., Matoba, S., and Aoki, T.: Initial field  
763 observations on Qaanaaq ice cap, north-western Greenland, *Ann. Glaciol.*, 55, 25–33.  
764 <https://doi.org/10.3189/2014AoG66A102>, 2014.

765 Takeuchi, N., Sakaki, R., Uetake, J., Nagatsuka, N., Shimada, R., Niwano, M., and Aoki, T.: Temporal  
766 variations of cryoconite holes and cryoconite coverage on the ablation ice surface of Qaanaaq  
767 Glacier in northwest Greenland. *Ann. Glaciol.*, 59, 21–30. <https://doi.org/10.1017/aog.2018.19>,  
768 2018.

769 Tanikawa, T., Hori, M., Aoki, T., Hachikubo, A., Kuchiki, K., Niwano, M., Matoba, S., Yamaguchi, S.,  
770 and Stamnes, K.: In situ measurements of polarization properties of snow surface under the  
771 Brewster geometry in Hokkaido, Japan, and northwest Greenland ice sheet. *J. Geophys. Res.*, 119,  
772 13,946-13,964. <https://doi.org/10.1002/2014JD022325>, 2014.

773 Tsutaki, S., Sugiyama, S., Sakakibara, D., Aoki, T., and Niwano, M.: Surface mass balance, ice  
774 velocity and near-surface ice temperature on Qaanaaq Ice Cap, north-western Greenland, from  
775 2012 to 2016, *Ann. Glaciol.*, 58, 181–192. <https://doi.org/10.1017/aog.2017.7>, 2017.

776 van As, D., Fausto, R. S., Ahlstrøm, A. P., Andersen, S. B., Andersen, M. L., Citterio, M., Edelvang,  
777 K., Gravesen, P., Machguth, H., Nick, F. M., Nielsen, S., and Anker, W.: Programme for  
778 Monitoring of the Greenland Ice Sheet (PROMICE): First temperature and ablation records, *Geol.*  
779 *Surv. Den. Greenl.*, 23, 73–76. <https://doi.org/10.34194/geusb.v23.4876>, 2011.



780 van den Broeke, M., van As, D., Reijmer, C., and van de Wal, R.: Assessing and improving the quality  
781 of unattended radiation observations in Antarctica, *J. Atmos. Ocean. Tech.*, 21, 1417–1431.  
782 [https://doi.org/10.1175/1520-0426\(2004\)021<1417:AAITQO>2.0.CO;2](https://doi.org/10.1175/1520-0426(2004)021<1417:AAITQO>2.0.CO;2), 2004a.

783 van den Broeke, M., Reijmer, C., and van de Wal, R.: Surface radiation balance in Antarctica as  
784 measured with automatic weather stations, *J. Geophys. Res.*, 109, D09103, 1–17.  
785 <https://doi.org/10.1029/2003JD004394>, 2004b.

786 van de Wal, R. S. W., Greuell, W., Van den Broeke, M. R., Reijmer, C. J., and Oerlemans, J.: Surface  
787 mass-balance observations and automatic weather station data along a transect near Kangerlussuaq,  
788 West Greenland. *Ann. Glaciol.*, 42, 311–316. <https://doi.org/10.3189/172756405781812529>, 2005.

789 Wehrli, C.: World Radiation Center (WRC) Publication. Davos-Dorf, Switzerland, 615, pp. 10-17,  
790 1985.

791 Wiscombe, W. J., and Warren S. G.: A model for the spectral albedo of snow. I, Pure snow. *J. Atmos.*  
792 *Sci.*, 37, 2712–2733., 1980.

793 Yamaguchi, S., Matoba, S., Yamazaki, T., Tsushima, A., Niwano, M., Tanikawa, T., and Aoki, T.:  
794 Glaciological observations in 2012 and 2013 at SIGMA-A site, Northwest Greenland. *Bull.*  
795 *Glaciol. Res.*, 32, 95–105. <https://doi.org/10.5331/bgr.32.95>, 2014.